ON ADAPTIVE IMAGE SEGMENTATION OF REMOTELY SENSED IMAGERY

AARON JONATHAN JUDAH

A THESIS SUBMITTED TO THE FACULTY OF GRADUATE STUDIES IN PARTIAL FULFILLMENT OF THE REQUIREMENTS FOR THE DEGREE OF MASTER OF SCIENCE

GRADUATE PROGRAM IN EARTH AND SPACE SCIENCE AND ENGINEERING
YORK UNIVERSITY
TORONTO, ONTARIO

October 2014

ABSTRACT

A critical step in object-oriented geospatial analysis (OBIA) is image segmentation. A single set of parameters is often not effective segmenting an image. To solve this problem, an adaptive approach to image segmentation has been proposed, which utilizes segments determined from a lower-spatial resolution image as the context to analyse a corresponding image at a higher-spatial resolution to create multiple sets of segmentation parameters to address the needs of different parts of the image. However, due to inherent differences in perceptions of a scene at different spatial resolutions and co-registration, segment boundaries from the low spatial resolution image need to be adjusted before they are applied to the high-spatial resolution image. This is a non-trivial task due to considerations such as noise, image complexity, and determining appropriate boundaries. Accordingly, an innovative method was developed. Adjustments were executed for each boundary pixel based on the minimization of an energy function characterizing local homogeneity. Adjustments are based on a structure which rewarded movement towards edges, and superior changes towards homogeneity. The adjusted segments act as the basis for the determination of segmentation parameters through a variogram based method. The developed method was tested on a set of Quickbird, and ASTER images, from a study area in Ontario, Canada. Results showed that the adjusted segmentation boundaries obtained from the lower resolution imagery were aligned well with the features in the Quickbird imagery, and segmentation maps determined using the adaptive segmentation method were superior to those created by a non-adaptive approach. This work will allow users to more easily and quickly segment large high resolution images.

ACKNOWLEDGEMENT

I have been very fortunate to work with Dr. Baoxin Hu in the Earth and Space Science and Engineering Department at York University. I would like to express my warmest thanks and gratitude to her for recognizing my potential and providing opportunities, encouragement, knowledge and support of the completion of this thesis.

I would also like to extend my appreciations to Dr. Jianguo Wang for his guidance, support, throughout this thesis. As well I would like to thank the other faculty members of the department for their support and contributions. They have all made my graduate studies an enriching experience.

I am also grateful for financial support provided by the Natural Sciences and Engineering Research Council (NSERC) of Canada. The ASTER data product was obtained through the online Data Pool at the NASA Land Processes Distributed Active Archive Center (LP DAAC), USGS/Earth Resources Observation and Science (EROS) Center, Sioux Falls, South Dakota (https://lpdaac.usgs.gov/data_access).

TABLE OF CONTENTS

LIST OF TABLES

LIST OF FIGURES

Chapter 1

INTRODUCTION

When analysing high spatial resolution (less than 5m) remotely sensed imagery, an important consideration is that pixel-based analysis may not be adequate [1,2] due to the fact that single pixels often represent only a small part of an object of interest (e.g. buildings, and tree crowns). An alternative which has been shown to outperform the pixel-based approach, to image analysis, is the object-oriented approach [1-3]. A key step in object-oriented image analysis is to segment an image into relatively homogeneous regions; these constitute what are often called image objects. The spectral, spatial, and textural features of these objects are then used for image analysis (such as classification) [1-3]. The accuracy and quality of object-oriented analysis rely heavily on the proper segmentation of the image. This has

driven the development of various segmentation techniques for remote sensing applications [1-8].

Existing segmentation methods can be generally grouped into two categories: edge-based and region-based [9]. With edge-based approaches, edges are usually generated first by an edge-detection algorithm and then using post-processing, adjusted to continuous boundaries that outline the resulting segments. These types of methods are sensitive to noise, and tend to over-segment an image. Region-based methods are built on using the similarity among pixels to form homogeneous regions in an image. Region growing is the commonly used technique in region-based methods. It starts with individual pixels as initial segments and subsequent merging of neighboring segments turns them into larger ones according to a pre-determined homogeneity criterion. In this way, closed regions are guaranteed to be created. In addition, with region growing methods, multiple features can be easily incorporated and the segments generated from edge-based methods can be used as initial segments as well. As a result, among the existing image segmentation methods, region-growing techniques are being widely used for remote sensing applications [2,9,10].

One of the issues with region growing methods is that they require a set of user-supplied input parameters to determine the segmentation process. These parameters need to be appropriately determined in order to generate image objects that best represent the features of interest. This is often done using trial and error, which is an inadequate, and imprecise. Also, one set of parameters may not be sufficient for the entire area covered by a large remotely sensed image. It is likely that the image contains objects with different sizes and characteristics. A single set of parameters often leads to under-segmentation of some parts of the image and over-segmentation of others. A demonstration of this argument is provided in Figure 1.1. For the segments in Figure 1.1 a region growing method using on one set of input parameters was applied to a Quickbird image (with a spatial resolution of 2.4 m by 2.4 m) over a forest scene. It is clear that some forest stands were over-segmented, while others were under-segmented.

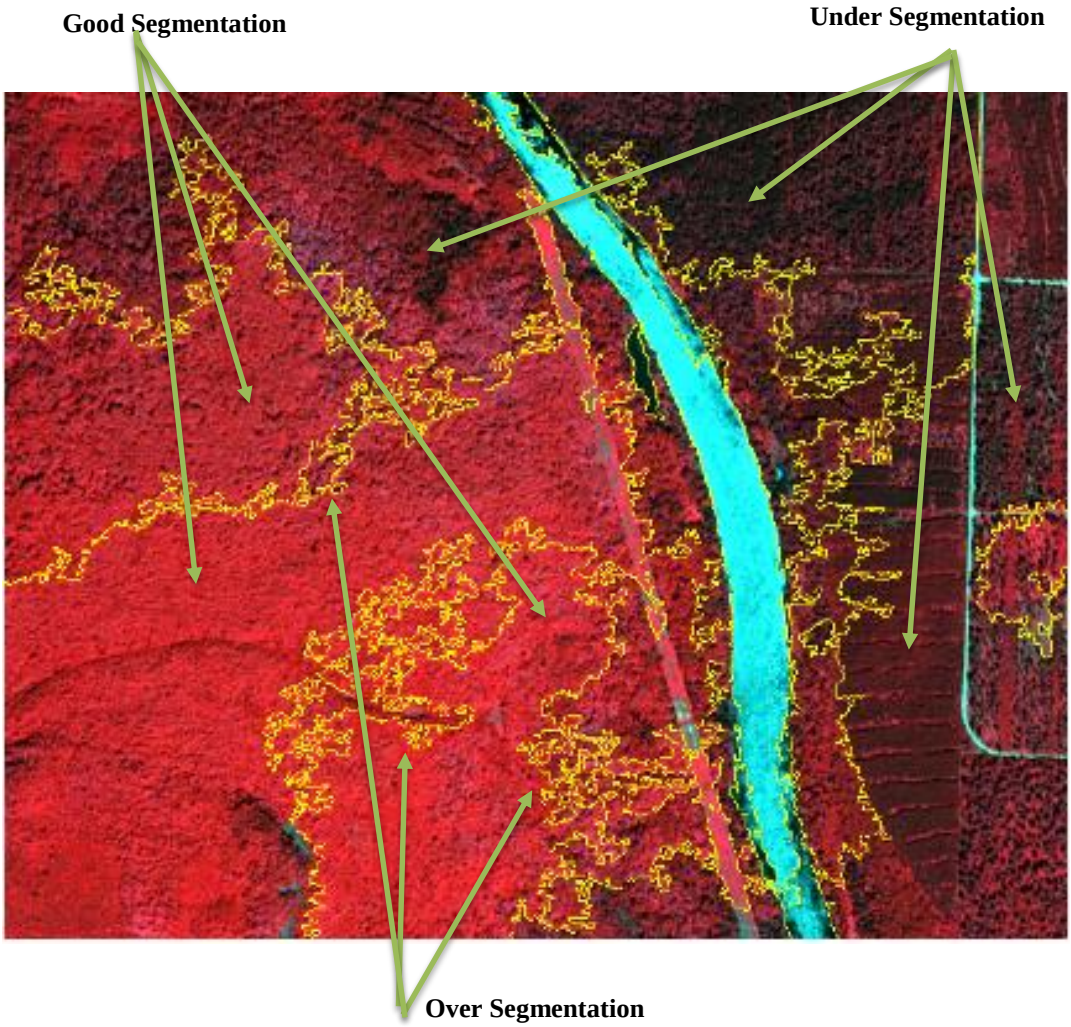

Figure 1.1. High resolution Quickbird image of a landscape segmented with a single set of segmentation parameters. Good, over and under segmentation is highlighted with green arrows.

The objective of this this thesis is to address the abovemention issues through the development of a region growing segmentation method for high-spatial resolution imagery [8]. The fundamental idea is to allow the segmentation parameters to vary from region to region across the whole image in an automatic fashion, based on the information acquired from a low-spatial resolution representation of the same area. The low-spatial resolution representation can be generated from the original high-spatial resolution imagery or from observations by different sensors. By analyzing a low resolution representation of a study area, coarser features of that area can be more easily identified, which can then be used to determine parameters for use in further analysis of those same areas on the corresponding high resolution imagery. In this way, over or under segmentation of the high resolution image can be avoided or minimized, and some level of consistency can be achieved between segmentation of different images. Furthermore, other imagery products, which may not be available in a high resolution form, such as surface temperature, could in principle be incorporated for further analysis.

One major challenge in implementing this idea is on how to adjust the segment boundaries obtained from low-spatial imagery to align well with features in corresponding high-spatial resolution imagery. This misalignment tends to be more

severe when data from different sensors are used. This drove the development of a methodology capable of refining segment boundaries, which is one of the key contributions of this master research, which has resulted in a publication [11].

A good physical analogy to the issue of boundary adjustment is the phenomenon of sand particles settling on a topographical feature. Suppose that a handful of sand is dropped on the top of randomly structured terrain. Under the influence of gravity, these particles would move to areas where the local potential energy is minimal. Based on the same principle, active contouring models were developed to outline objects in computational vision research [6,12,13,14,15]. Active contours, also known as snakes, are energy-minimizing curves that evolve from their initial positions to fit image features, such as edges and lines, under the influence of image determined forces and external constrains. Active contour methods are classically defined as a curve which is attracted to image features such as edges, lines, or corners[15]. This attraction is quantified by an energy function, which has low values in places on the image which contain those desired features. The energy function also incorporates a term that depends on the shape of the curve and can be used to bias the curve to take on smooth shapes, and a term that depends on user

interaction, so that the curve can be interactively pulled toward a desired location [15].

Different energy functions for boundary adjustment have also been reported in the literature. Some are based on image gradients (edge-based active contouring models), while others on statistics of the image objects and the background (region-based active contouring models). Region-based active contouring models do not depend on image gradients and thus are less susceptible to noise and work well for objects with weak boundaries. Active contour methods for boundary adjustment or boundary detection, have been used successfully in the field of medical imaging to detect contrasting regions, such as different tissue types [12,16,17,18], and in some remote sensing applications [10,14,19]. Some drawbacks of utilizing active contour methods include their susceptibility to noise [15,20,21], difficulty with complex images [12,15,21,22], and difficulty in implementing the method when multiple boundaries are present or when boundaries cross [15,22,23]. In addition, traditional active contour methods utilize a single set of operating parameters which can limit its ability to recognize multi-scale features in an image [19,20].

For our specific situation, we wish to adjust boundaries in a large, complex image, with multiple boundaries, while trying to maintain the local nature of those boundaries. To achieve this, we adopt the concept of energy-minimization to refining segment boundaries through a new energy function which considers image gradients and regional statistics and we also designed an implementation strategy for the adjustment. Our proposed energy function is similar to traditional active contour energy functions in that the boundary is attracted towards desired features, and is minimized at desired image locations but is unique in that it does not rely on the curvature of the boundary, incorporates homogeneity, and it is explicitly local.

In summary, in order to improve the segmentation of high spatial resolution remotely sensed imagery, we developed an adaptive, semi-automatic, and multi-scale approach. This method utilized a low-resolution representation of a study area to aid in the segmentation of a high resolution image of that same area. The method operated by first segmenting the low-resolution representation, using a region growing method, and then projecting it onto the high-resolution image. This projected segment map then had its boundaries adjusted using a method developed for this thesis. Once adjusted, these projected, adjusted, segments were then

analysed with a variogram based method to determine a set a parameters to further segment these areas using a region growing method.

This thesis is broken into 7 chapters. Chapter 1 contains an introduction and overview of the developed segmentation method. Chapter 2 covers the fundamentals of region growing segmentation, the characterization of the spatial variation of a scene using variograms, and the assessments of segmentation results. Chapter 3 presents the developed methods for adaptive segmentation and boundaries adjustment. In Chapter 4, the results will be presented and in Chapter 5 evaluations of those results will be described. The closing remarks and future work will be presented in Chapter 6, with Chapter 7 is the

Chapter 2

TECHNICAL BACKGROUND

In this chapter the technical details and the general concepts behind several algorithms and methods used in this thesis will be presented. The first section will provide background on the different types and classifications of remote sensing products which are presently available. The second section will provide the background on the region growing algorithm which was used throughout this thesis. The next section will cover the methodology used to characterize the spatial variation of a remotely sensed image. The last section of this chapter will cover F-measure which is a quantitative measure used to evaluate the quality of a segmentation result.

2.1. REMOTELY SENSED IMAGERY AND THEIR APPLICATIONS

In this section a brief primer on the different types of remotely sensed imagery and their common uses will be presented. Some terminology which is specific to remote sensing needs to be defined. When referring to the source of the remotely sensed imagery, the source is often referred to by the trade name of the sensor which produced it. There is a distinct difference between the actual satellite which carries the sensor, and the sensor itself which collects the imagery. It is not uncommon for a satellite to carry more than one sensor, so the satellite itself can be the source of multiple imagery sources. Remotely sensed imagery is classified based on its resolution. It is generally agreed that remotely sensed imagery can be classified into 5 categories. Very low resolution (<100m), low resolution (100m to 15m), medium resolution (~15m to 5m), high resolution (5m to 1m), and very high resolution (<1m) [24]. Common uses and features for each category of remotely sensed imagery are as follows.

Very low resolution (<100m)

These products are generally used in climate change analysis and for assessing changes caused by large scale events such as natural disasters. This includes forest fires, floods, hurricanes etc. Some of these products have daily coverage of the entire planet, which is driven by the high orbit of the satellite and the large foot print of the imagery, in some cases almost 1000 km by 1000 km. These products also offer cloud free composites as a standard product which are created from the "stitching" of a time series of images, removing clouded areas and replacing them with cloud free acquisitions [24]. These products are almost always multi-spectral in nature and contain bands spanning the visual to the thermal IR areas of the spectrum. Very low resolution imagery includes the MODIS, AVHRR, and Meteosat series of satellite sensors [24].

Low Resolution (100m to 15m)

A common use for these images are the detection of land cover changes due to anthropogenic actions such as the expansion of cities, industrial levels of vegetation harvesting and overall industrialization of a landscape. These products are almost always multi-spectral with bands spanning from the visual to the thermal IR areas of the spectrum. These products have global coverage but have an acquisition time which is generally measured in weeks rather than days. This is driven by the high orbit and relatively small footprint (at most several hundred km by several hundred km) of the imagery [24]. Imagery products which are considered to be low resolution include LANDSAT ETM+, LANDSAT MSS, and ASTER series of satellites [24].

Medium Resolution (~15m to 5m)

Medium resolution imagery is a common imagery resolution of several commercial imagery products such as RapidEye, IRS, and SPOT [23,25]. These imagery products tend to have less spectral bands than low and very low resolution imagery

products. The spectral bands for these products are mostly centered in the visual area of the spectrum and have limited IR capabilities. These products are useful in the identification and of complex and large buildings or industrial areas, and the extents of natural land features such as shorelines and cliffs. These products have global coverage and the acquisition time for these products are measured in weeks. The foot print for each acquired image are measured in 10's of km, with the orbit of the source satellite is comparable to those of the low resolution imagery products.

High Resolution (~5m to 1m)

High resolution imagery products are primarily used in the identification of objects such as trees, smaller buildings, and such as vehicles. High resolution imagery are often used in applications such as forest and agricultural management. These images are almost always multi-spectral with their spectral range limited to visual bands and some areas of the IR spectrum. It is rare that these images have thermal properties. These images are of relatively small foot print of several km by several km. Added in with the low orbit of the satellites which carry these high resolution sensors, the

return fly over time is measured in many weeks. High resolution imagery sources include Quickbird, Geoeye, and world view [7,24,25].

Very High Resolution (<1m)

Very high resolution imagery, from satellite based sources, is generally not available to the public and is the domain of recognisance satellites which are designed and fielded by the governments of a handful of nation states. The design and specifications of the sensors, which produce these images, are largely classified but it is generally agreed that the images produced by these satellites are optimized to the visual range of the spectrum with limited capabilities in the IR region [26]. These images trade spectral range for superior spatial detail. As an example these images are capable of identifying individual vehicles, and in some cases, the make of vehicle. It is rumored that that for some of the most advanced satellites, on a clear cold day, are capable of discerning details such as the logo markings or other identification marks on aircraft and vehicles. Figure 2.1 provides a visual representation of how different a scene can look at different levels of high resolution [25,26].

0.10m Resolution

0.25m Resolution

0.50m Resolution

1.00m Resolution

Figure 2.1. The same scene represented under different high resolution observations, ranging from 0.10m, 0.25m, 0.50m, and 1.00m.

2.2. REGION GROWING IMAGE SEGMENTATION

A region growing algorithm based on Baatz [27] was utilized throughout the segmentation method. In essence, a region growing algorithm determines if pixels or groups of pixels should be grouped together based on some pre-determined criteria, and then carries out those groupings if appropriate. This is an iterative process and it is terminated once merges between segments ceases. Shown in Figure 2.1 is an example of the merging processing of region growing segmentation. For clarification, we denote the base IO (image object) as the object which is used to determine the location of neighbors which could be merged into it; and the neighbor IO(s) as the IO that surround the base IO. In Figure 2.1, the base IO is represented by the light blue cells labeled 'B'; and the neighbor IOs are the pixels in colors green, red, and dark blue pixels, labeled 1, 2, and 3.

These neighbor IOs are to be examined in order to determine the best fitting one to merge with the base IO based on a defined measure and a corresponding threshold value which is used to determine the extents of the segmentation. With the best fitting neighbor IO, if a pre-determined merging threshold is met, this neighbor IO is selected as a *possible* candidate to merge with the base IO, now called the merging

candidate. In Figure 2.2 this is represented by the red region labeled 2. The final check of merging suitability involves checking if the merging candidate is best suited to merge with the base IO. This is determined by establishing the suitability of merging of the IO to its neighbors, which includes the base IO. In Figure 2.2 the red region labeled with 2, has its neighbors identified and compared which are regions which are green, light blue, dark blue, yellow, and purple, numbered 1, B, 3, 4, and 5. If it is determined that the base IO, is in fact, the most suitable IO to merge with the merging candidate, only then is the merging candidate merged to the base IO. This second check of the merging IO candidate to its neighbors is to ensure the best fitting is mutual. In Figure 2.2 (C) region B and 2 have been combined, indicated by their mutual light blue colour.

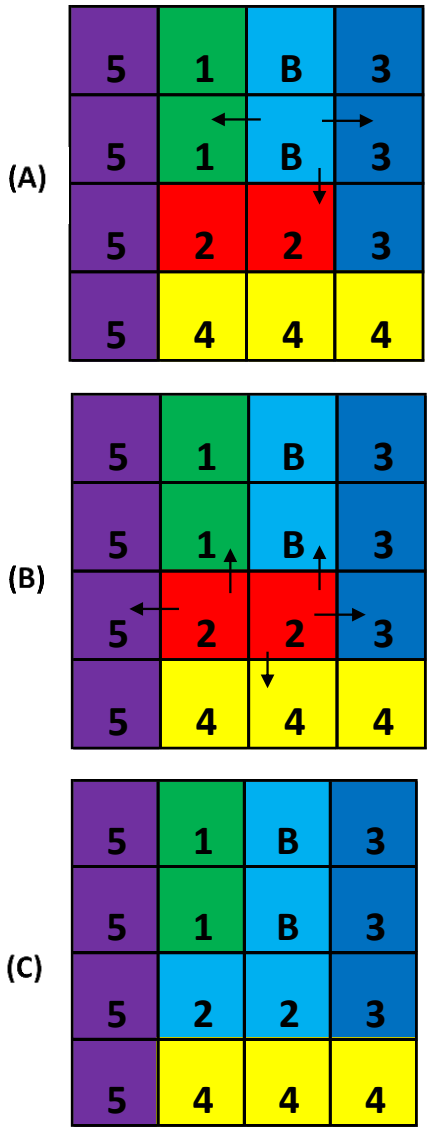

Figure 2.2. Example of a region growing merging operation. B represents the base pixels, pixels numbered 1 to 5 represents the neighbor pixels.

This process is repeated until all pixels have been scanned, and is iterated until merging has ceased.

The core to any region growing segmentation is to determine the measure of fitting and the merging threshold. In the following, commonly used measures to calculate the degree of fitting between two IOs will be described. Given a feature space of d-dimension, the degree of fitting between two IOs can be calculated based on Euclidean distance defined in (2.1).

$$h = \sqrt{\sum_{d} (f_{1d} - f_{2d})^2} \tag{2.1}$$

f_{1d} is the value of the feature space for the given image object 1 while f_{2d} is the value of the feature space for image object 2, for feature space of *d* dimensions. This similarity measure is essentially the distance of the feature space between two image objects. This distance measure can be further standardized by integrating the standard deviation over all IO's of the features in each dimension:

$$h = \sqrt{\sum_{d} \left(\frac{f_{1d} - f_{2d}}{\sigma_{fd}} \right)^2} \tag{2.2}$$

The above measures are good for comparisons where finding commonalities in spectral signature are of interest. A limitation of these measures are that they do not take into account the statistical heterogeneity of the region leads to the sizes or shapes of IOs. Since the goal of segmentation is to maximize inter-segment homogeneity and intra-segment heterogeneity, merging of IOs should be done such that the merge results in the minimum increase in heterogeneity. To reflect this, Baatz [23] proposed to calculate the degree of fitting through the difference in the before and after measures of heterogeneity (*h*). When executed Baatz utilized standard deviation for the homogeneity measure as did other authors who implemented Baatz's measure [28,29,30].The degree of fitting is defined as h_{diff}:

$$h_{diff} = h_m - \frac{h_1 + h_2}{2} \tag{2.3}$$

h_m is the homogeneity measure of the merged image objects, while h_1 and h_2 are the homogeneity of the two individual image objects before merging. Homogeneity can be measured through any number of statistical definitions such as spectral means, variance or standard deviation. For this thesis variance was chosen because it is more physically representative of the system it is describing, in this case IOs and their homogeneity. From hereafter σ^2 will be used in place of *h*. Since variance is in square units it is more physically similar to IOs which by definition encompass areas. This definition is also called the Ward's Criterion [31]. The concept considers the model error for a region. The dissimilarity associated with a pair of regions is defined as the additional total error that is introduced by merging the two regions. This can be expressed as:

$$\sigma^2{}_{diff} = (n_1 + n_2)\sigma^2{}_m - (\sigma^2{}_1 n_1 + \sigma^2{}_2 n_2) \tag{2.4}$$

Where n_1 and n_2 are the number of pixels in each IO which are to be merged, n_m is the number of pixels in the proposed merged IO, $\sigma^2{}_m$ is the variance of the proposed

merged IO, ${\sigma^2}_1$, and ${\sigma^2}_2$ are the variances of the IO to be merged, and ${\sigma^2}_{diff}$ is the weighted, variance difference.

(2.4) can be generalized for an arbitrary number of channels c, each having an individual weight (w_c):

$$ {\sigma^2}_{diff} = \sum_c w_c \left(n_1 ({\sigma^2}_{mc} - {\sigma^2}_{1c}) + n_2 ({\sigma^2}_{mc} - {\sigma^2}_{2c}) \right) \tag{2.5} $$

The measure of degree of fitting defined by [27] is what is utilized by the commercial software suite Definiens, which is widely used in the analysis of remotely sensed imagery.

Incorporating the shape of IOs can also be used in evaluating possible merges. The following two definitions of shape homogeneity are utilized by the Definiens software suit and are described by Baatz [27]. One measures the deviation from the

ideal compactness, and the other is the deviation from the shortest possible edge length given by the bounding box of a segment, otherwise known as smoothness. The homogeneity of compactness is defined as:

$$h_{cmp} = \frac{l}{\sqrt{n}} \tag{2.6}$$

l is the edge length, and *n* is the object size in pixels. Otherwise saying it is the ratio of the edge length to the length of a square with *n* pixels. The homogeneity measure of smoothness is given by:

$$h_{smt} = \frac{l}{b} \tag{2.7}$$

b is the shortest possible edge length determined by a bounding box of the segment, while *l* is the factual edge length of the IO. In a raster the edge length of the bounding

box is also the shortest possible edge length for an arbitrary segment, such that $l>b$ holds for any image object. Incorporating these shape homogeneity measures can be done simply by their weighted addition to the homogeneity measure associated with that particular IO:

$$\begin{aligned}\sigma^2{}_{diff_{shp}} = \sum_c w_c\left(1-w_{shp}\right)\left(n_1(\sigma^2{}_{mc}-\sigma^2{}_{1c})\right.\\ +n_2(\sigma^2{}_{mc}-\sigma^2{}_{2c})\big)+w_{shp}\big\{\big(1-w_{cmp}\big)\big(\sigma^2{}_{smt_{mc}}\\ -\sigma^2{}_{smt_{1c}}\big)+w_{cmp}\big(\sigma^2{}_{cmp_{mc}}-\sigma^2{}_{cmp_{1c}}\big)\\ +\big(1-w_{cmp}\big)\big(\sigma^2{}_{smt_{mc}}-\sigma^2{}_{smt_{2c}}\big)\\ +w_{cmp}\big(\sigma^2{}_{cmp_{mc}}-\sigma^2{}_{cmp_{2c}}\big)\big\}\end{aligned} \tag{2.8}$$

Following the previous definitions, additional variables are defined: w_{shp} is the weighting of the shape factor versus spectral homogeneity, w_{cmp} is the weighting of compactness versus smoothness, $\sigma^2{}_{smt\_mc}$ is the smoothness factor of the merged IO for channel c, $\sigma^2{}_{cmp\_mc}$ is the compactness factor of the merged IO for channel c, $\sigma^2{}_{smt\_xc}$ is the smoothness factor for IO *x* for channel c, and $\sigma^2{}_{cmp\_xc}$ is the

compactness factor for IO *x* for channel c. For this project the shape factor was incorporated into the region growing program, although it was not always used during testing.

2.3. CHARACTERIZATION OF THE SPATIAL VARIATION OF A SCENE IN REMOTELY SENSED IMAGERY

In order to automatically determine the merging threshold in region growing, according to the definition described by (2.5) it is important to characterize the spatial distribution of the dominant objects in the image scene. A number of studies have successfully used variograms to characterize the spatial structures of observed surface properties [32-35]. Using variograms studies have been able to successfully describe the nature and the causes of spatial variation within an image [35] such as radiometric contrast between the image objects, and the mean size of the image objects [35,36,37]. Furthermore other studies have shown that variograms can successfully quantify the spatial heterogeneity components (spatial variability and spatial structure) of the landscape [38]. The variogram, a function describing the

degree of spatial dependence of a stochastic process, is commonly used [33,34,35]. According to the similarity measure described by (2.5) variogram analysis, in principle, can be used to automatically determine parameters which can be used in the segmentation of an image. In order to calculate the variogram, each spectral band in a remote sensing image is treated as a 2D dataset with spatial variances determined by spectral intensities, and the numerical location difference between pixels acting as the spatial distance between data points. More specifically it can be write this out as:

$$\Gamma(h) = \frac{1}{2n}\sum_{i=1}^{n}[z(x_i) - z(x_i + h)]^2 \tag{2.9}$$

$\Gamma(h)$ is the variogram value for a pixel distance (also known as a lag distance), h. n is the number of instances of h, $z(x)$ is the intensity value at a pixel with coordinate vector (x). Here $\Gamma(h)$ is an unbiased estimate of the population variance, and describes the dissimilarity between spatially distributed regionalized variables, otherwise known as the variance. The larger the $\Gamma(h)$, implies that pixels at the corresponding lag distance are less similar. From a physical standpoint an

experimentally determined variogram is an empirical estimate of the variance of a Gaussian process.

When applying equation (2.9) to an image, a profile similar to that of Figure 2.3 can be created. Most variograms are defined through several parameters; namely the nugget effect, sill, and range. These parameters are depicted on the generic variogram shown in Figure 2.3 and are defined as follows:

- Nugget effect (c_o) – represents micro-scale variation or measurement error. It is estimated from the empirical variogram as the value of $\Gamma(h)$ for h=0.
- Sill (c) – the $lim_{h\to\infty}\Gamma(h)$ represents micro-scale variation or measurement error.
- Range (a) – the distance (if any) at which data are no longer autocorrelated. For variogram models with an asymptotic sill, it is conventionally taken to be the distance when the variance first reaches 95% of the sill.

Patterns of variance against lag distance that do not increase monotonically to the sill can indicate the presence of cyclic spatial structures or multiscale patters within the image.

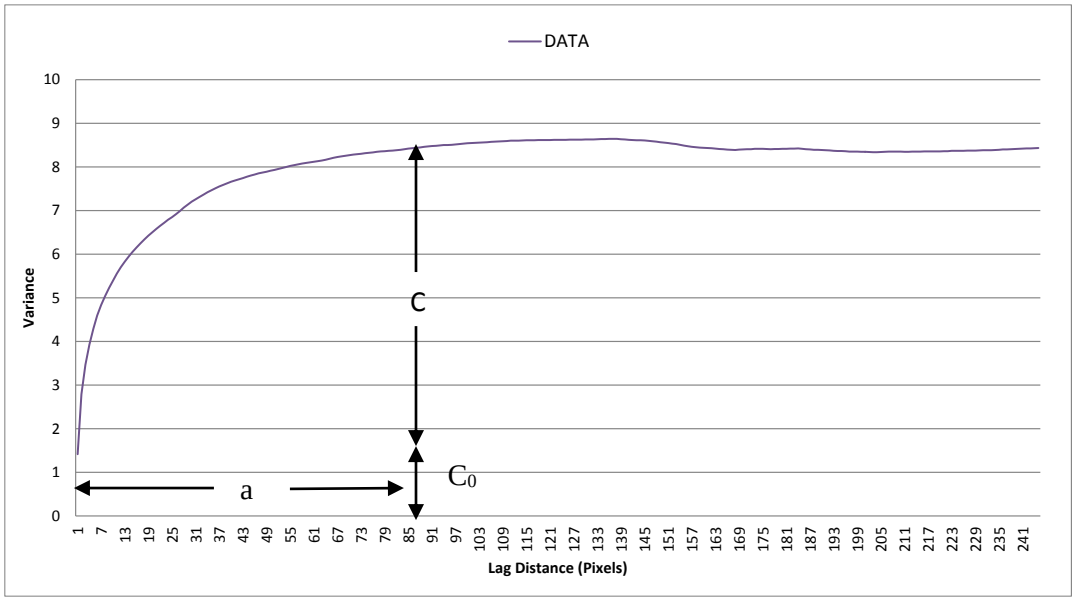

Figure 2.3. Diagram of the variogram by lag value, illustrating the features of nugget, sill, range.

In Figure 2.3 the variables *a*, *c*, and c_o are defined but in order for these variables to be characterized a mathematical relationship needs to be applied, such as the one defined by the spherical model expressed by Chen and Jiao [44].

$$\begin{cases} \Gamma(h) = c_o & \text{when } h=\varepsilon \\ \Gamma(h) = c_o + c\left(\frac{3h}{2a} - \frac{h^3}{2a^3}\right) & \text{when } 0<h\leq a \\ \Gamma(h) = c_o + c & \text{when } h>a \end{cases} \tag{2.10}$$

In order to fit the model described by (2.10) linear programming techniques were used to solve for the variables. (2.9) is re-written for the instance when $0<h\leq a$.

$$\Gamma(h) = c_o + \left(\frac{3c}{2a}\right)h + \left(-\frac{c}{2a^3}\right)h^3 \tag{2.11}$$

The following substitutions are performed:

Original Variable	$\Gamma(h)$	$\frac{3c}{2a}$	$\frac{c}{2a^3}$	c_o	H	h^3
Replacement Variable	B	x_1	x_2	a_1	a_2	a_3

Table 1. Variable substitutions for solving the spherical equation using linear programming.

Using the substitutions in Table 1 the following linear equation is produced:

$$b = a_1 x_1 + a_2 x_2 + a_3 x_3 \tag{2.12}$$

n(h) denotes observations of lag distance h_i and $\Gamma(h_i)$ denote the experimentally determined variogram value at lag h_i, for i = 1, 2,…, n, measurements of the variogram. Using the linearized form expressed by (2.12) experimental values can be substituted to yield:

$$\begin{aligned} a_{11}x_1 + a_{12}x_2 + a_{13}x_3 &= b_1 \quad && \text{when lag} = h_1 \\ a_{21}x_1 + a_{22}x_2 + a_{23}x_3 &= b_2 \quad && \text{when lag} = h_2 \\ &\cdots \quad && \cdots \\ a_{n1}x_1 + a_{n2}x_2 + a_{n3}x_3 &= b_n \quad && \text{when lag} = h_n \end{aligned} \tag{2.13}$$

This can be written out in matrix form.

$$Ax = b \tag{2.14}$$

Where:

$$A = \begin{bmatrix} a_{11} & a_{11} & a_{11} \\ a_{21} & a_{21} & a_{21} \\ \cdots & \cdots & \cdots \\ a_{n1} & a_{n1} & a_{n1} \end{bmatrix}, x = \begin{bmatrix} x_1 \\ x_2 \\ x_3 \end{bmatrix}, b = \begin{bmatrix} b_1 \\ b_2 \\ \cdots \\ b_n \end{bmatrix} \tag{2.15}$$

By applying objective function solving techniques, which minimizes the function through linear programming, a solution is yielded, which can be applied to determine the values laid out in (2.11). It should be noted that since (2.15) is in matrix form it is position well for parallel solving techniques for more efficient processing.

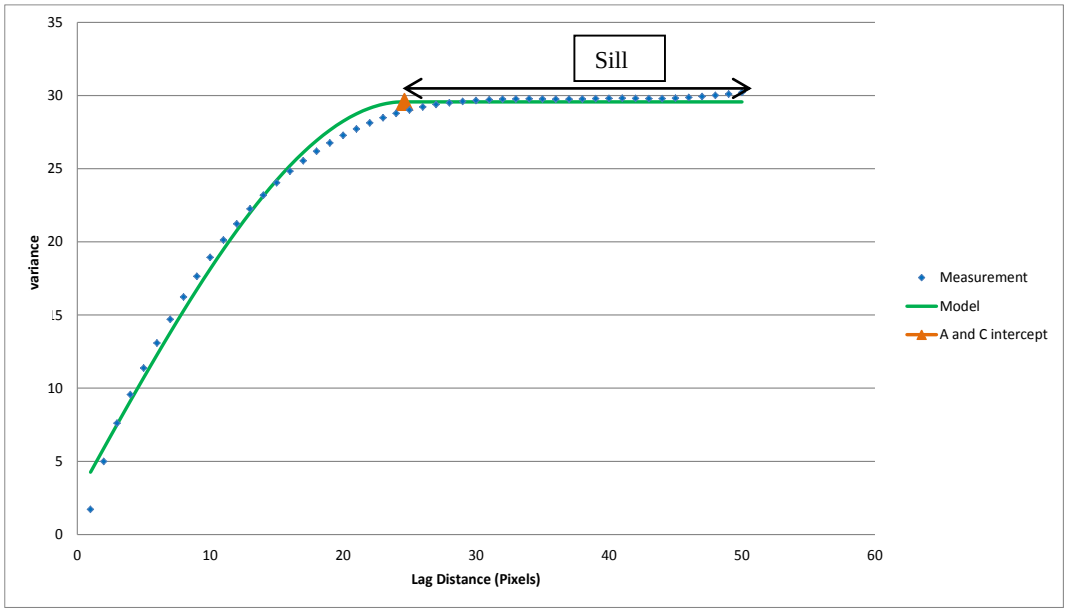

Figure 2.4. Example of the spherical model fitted to a set of variogram data using a linear programing fitting method. Portion known as the sill illustrated.

Figure 2.4 acts as an example of when the spherical variogram model is fitted to a set of data. The orange marker illustrates the point where a and $C + C_o$ intercept.

2.4. QUANTITATIVE EVALUATION OF SEGMENTATION – F-MEASURE

In order to quantify the performance of a segmentation result, a popular technique called F-measure, described by Estrada and Jepson [43] was used. In order to determine the F-measure of a segmentation result, the *precision* and *recall* of that result needs to be calculated. Mathematically, precision and recall are defined in equations (2.16) and (2.17), respectively. Given a segmentation map generated through a segmentation algorithm (called from here on in the reference segment map) $S_{reference}$, and a target segmentation map, S_{target}, created through human interpretation, precision is defined as the proportion of boundary pixels in $S_{reference}$ for which we can find a matching boundary pixel in S_{target}.

$$Percision = \frac{Matched(S_{reference}, S_{target})}{total(S_{reference})} \tag{2.16}$$

Where $total(S_{reference})$ is the total number of boundary pixels in a given reference segment map, and $Matched(S_{reference,}\ S_{target})$ is the total number of matched pixels from the reference segment map to the target segment map. In a similar way, recall

is defined as the proportion of pixels in S_{target} for which we can find a suitable match in $S_{reference}$.

$$Recall = \frac{Matched(S_{target,S_{reference}})}{total(Starget)} \tag{2.17}$$

In order to determine how pixels from either the target or source map match to one another, a matching algorithm also described by Estrada and Jepson [43] was used. For each boundary pixel $P = (X_p,Y_p)$ to be matched, a circular window of a radius, r, centered at (X_p,Y_p), any boundary pixels, from the other map, within this window are potential matches for P. A boundary pixel Q within the search window is a suitable match for P if the following conditions are satisfied:

(1) There are no other boundary pixels in $S_{reference}$ between P and Q (no intervening contours constraint)

(2) The reference pixel that is closets to Q and the source pixel P being matched to Q must be on the same side of the target boundary Q (same side constraint).

Once precision and recall are calculated, F-measure, which is a harmonic average of the two, can be calculated by:

$$F - measure = 2\frac{precision \cdot recall}{precision + recall} \quad (2.18)$$

Chapter 3

ADAPTIVE IMAGE SEGMENTATION METHODOLOGY

This chapter will begin with an overview of the imagery used in this thesis, and then a description of the adaptive segmentation method. Next the boundary adjustment method will be described. The boundary adjustment method can be broken down into 3 main steps. 1) Segmentation of the low resolution imagery, 2) projection and adjustment of the low resolution determined segments onto the high resolution imagery and 3) segmentation of each individual projected and adjusted segments. The adjustment method is a core aspect of this thesis and reflects the vast majority of the work done over the course of this project.

3.1. IMAGES USED

The developed methodologies were tested on a high-spatial resolution (2.4 m by 2.4 m) Quickbird [7] image over a study area in Ontario, Canada, shown in Figure 3.1. Quickbird provides 4 bands of information, blue (450-520 nm), green (520-600nm), red (630-690 nm), near-IR (760-900 nm) at 2.4 m resolution and also a 0.6 m panchromatic band [7], which was not used in this thesis. Two types of low spatial resolution images were also used to provide contextual information to segment the Quickbird image: a resampled Quickbird image (resampled to 15 m by 15m) and an ASTER (Advanced Spaceborne Thermal Emission and Reflector Radiometer) [45] image at a spatial resolution of 15 m by 15 m. The resampled Quickbird image perseveres the band information from the original Quickbird imagery, while the ASTER imagery provides 3 bands: green (520-600 nm), red (630-690 nm), and NIR (760-860 nm). The resampled Quickbird image was created by resampling the high resolution Quickbird image using a gaussian filtering method with a 5 by 5 window in order to reduce the 2.4m resolution Quickbird image to approximately 15m by 15m resolution of the ASTER image. The low spatial resolution imagery is shown in Figure 3.2. These images were chosen because of the varying landcover types present in the images and the fact that it covers a relatively large area of land (4.6km by 2.3 km).

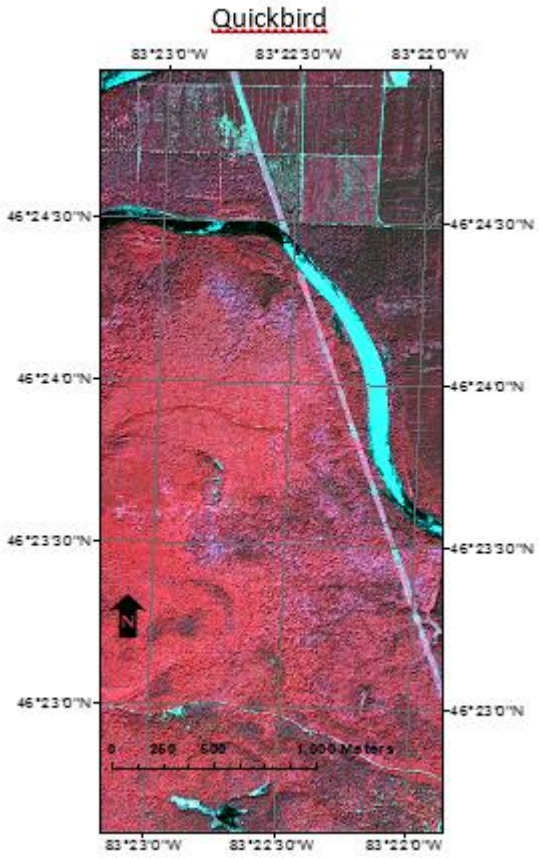

Figure 3.1. False colour composite of the Quickbird image with the near-infrared, red, and green bands displayed as red, green, and blue, respectively.

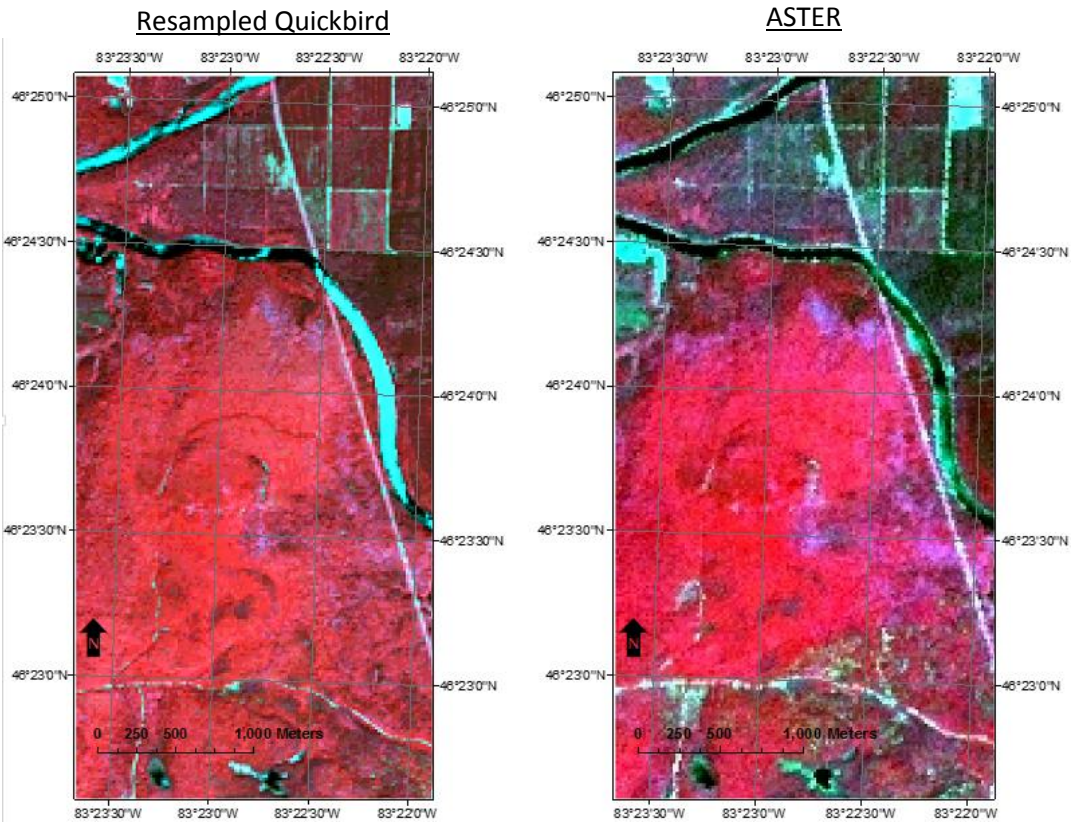

Figure 3.2. The false colour composite of the ASTER (right), low resolution resampled Quickbird (left), images over the same site with the near-infrared, red, and green bands displayed as red, green, and blue, respectively.

	Resolution	Acquisition date	Solar Zenith Angle	Solar Elevation Angle	Available Spectal Bands	Spectral Range (nm)
Quickbird	2.4m	17-Jul-07	63.520	157.450	4	450 to 890
ASTER	15m	31-Aug-10	63.758	147.468	14	520 to 11,650

Table 2. Summary of key features of both the Quickbird and ASTER image acquisitions.

3.2. THE ADAPTIVE IMAGE SEGMENTATION METHODOLOGY

An overview of the operation of the adaptive segmentation method is illustrated in the following flowchart:

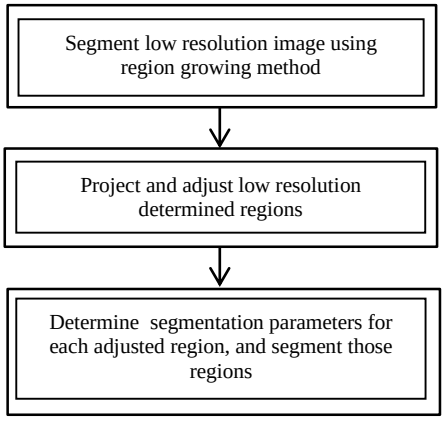

Figure 3.3. Flowchart illustrating our overall segmentation strategy.

The first step in the proposed segmentation method involves segmenting the ASTER image using the region growing method. The segmentation parameters used in this step were determined, in part, through variogram based analysis and user skill. The segments in the low resolution image correspond to areas on the higher resolution Quickbird image, which are then further characterized in order to determine individual threshold factors for further segmentation, if necessary. This initial ASTER determined segmented map was then dilated in size to match the extents of the Quickbird image. This ASTER determined, Quickbird projected segmentation map then had these initial regions undergo an adjustment determined by the algorithm outlined in the next section. Once adjustment was completed, a variogram based method analyzed the adjusted regions and determined scale values using both automatic and manual determinations, for use in segmentation, of those regions. These threshold values were then utilized in the segmentation of the areas within those boundary adjusted regions of the Quickbird image, using the identical region growing method utilized to segment the ASTER image. Once segmentation of the Quickbird image was complete, the segmentation process was considered completed.

During the development of the segmentation method it was observed that when segment boundaries determined from lower resolution imagery was compared to its positions on its corresponding high resolution imagery these segments would relate to forest-stands. If these segments were to be projected onto its corresponding high resolution imagery, the pixels which these segments encompass could be further analyzed to determine homogeneity parameters for more complete segmentation of the Quickbird image. This concept of using information gleaned from a lower resolution image to segment its corresponding high resolution counterpart forms the basis of the segmentation method presented in this thesis. To further explore this concept a low resolution image was segmented, and then projected onto its corresponding Quickbird image, shown in Figure 3.4 and Figure 3.5. As expected, the segments determined from the ASTER and resampled Quickbird image, called the projected segments hereafter, encompass larger features on the Quickbird image, and as an added effect did not match well to the features on the image. As part of the multi-scale image segmentation strategy, adjusting these boundaries to better match the features on the high resolution image would also be necessary for the developed methodology to be successful.

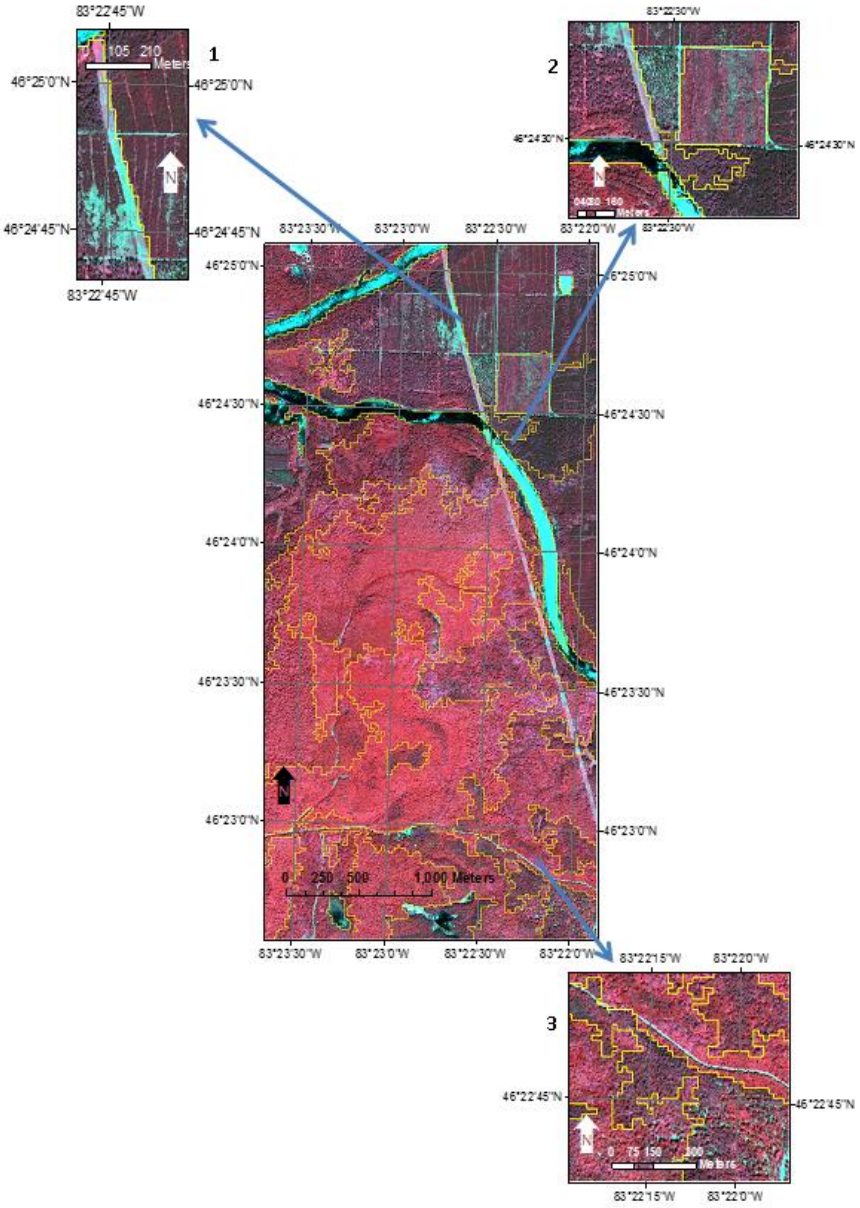

Figure 3.4. Segments determined from lower resolution resampled Quickbird imagery projected onto Quickbird imagery. The Quickbird image is displayed with the near-infrared, red, and green bands as red, green, and blue, respectively. Yellow lines represent segment boundaries.

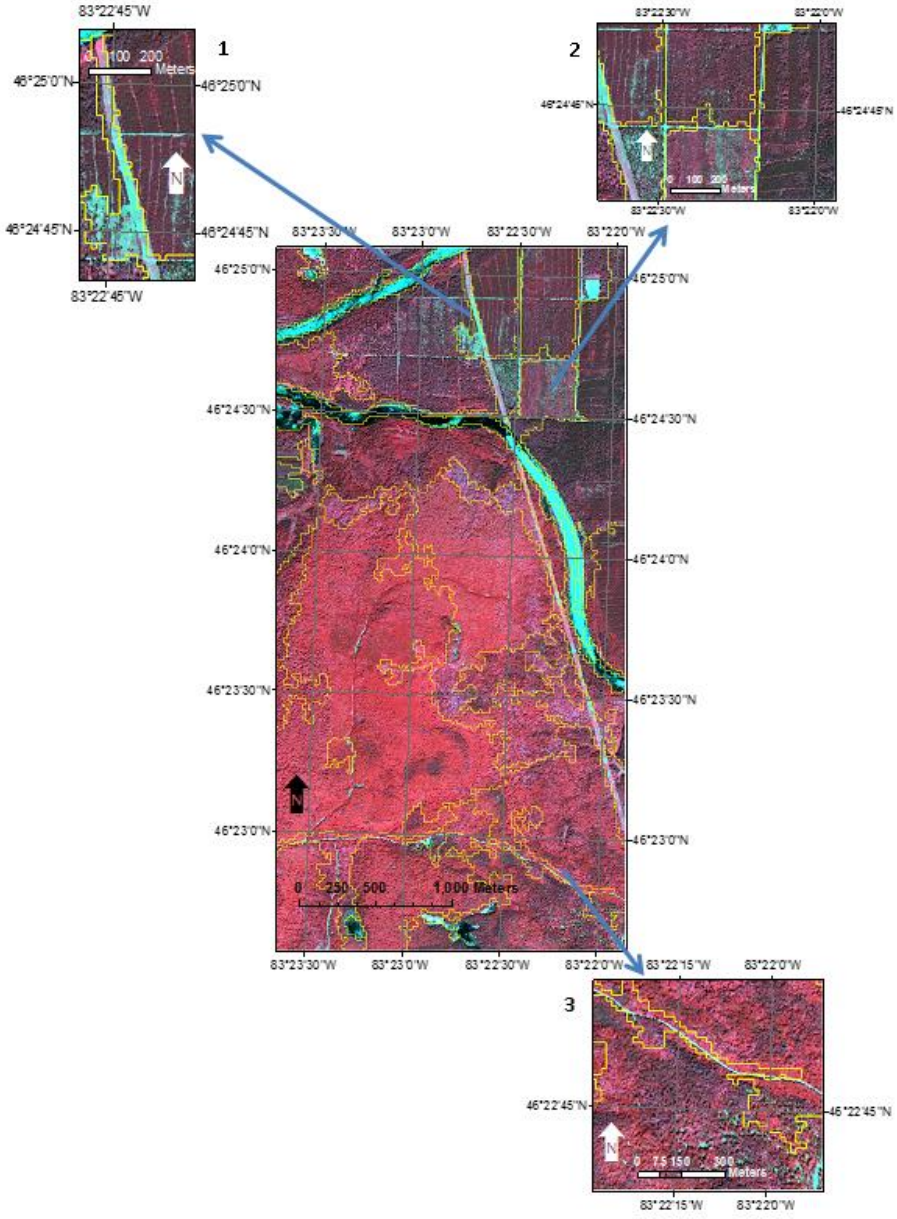

Figure 3.5. Segments determined from ASTER imagery projected onto Quickbird imagery. The Quickbird image is displayed with the near-infrared, red, and green bands as red, green, and blue, respectively. Yellow lines represent segment boundaries.

3.3. SEGMENTATION OF LOW RESOLUTION IMAGERY AND DETERMINING SEGMENTATION PARAMETERS FROM VARIOGRAMS

The first step in the adaptive segmentation process is the segmentation of the low resolution imagery. The parameters used in this process were determined in part through variogram analysis. In order to determine these factors from the variograms, created from the images, the variables defined in Table 1 were determined. From here a threshold value, defined by the Wards measure, to be used in the segmentation process was calculated. In the context of region growing, threshold can be thought of as the maximum modeled error for a merged region as expressed by the Ward's criterion [31]. In region growing, threshold corresponds to the fitting measure described by (2.5). When determining the value of this threshold, as a nominal relationship we yield:

$$threshold = f(V, d) \tag{3.1}$$

Where V is the variance determined from the sill of the variogram, and d is a length in pixels of the range of the sill. In essence, a threshold is a function which is a

product of both the homogeneity and the physical size of a projected IO. According to variogram analysis, a threshold value computed from the sill, will correspond to IO's which are likely to be present in the image. Threshold values computed from areas corresponding to positions beyond the sill are indicative of IO's which are not as likely to be present in the image. If region growing image segmentation is conducted using a threshold determined through this method, IO's should be produced to reflect these input values. Keeping these thoughts in mind and the variable definitions from the spherical model of the variogram, the threshold value based on variogram features is defined as:

$$threshold = (c + c_o) * a \tag{3.2}$$

3.3.1. EXAMPLES OF VARIOGRAM BASED ANALYSIS OF IMAGES

In this section several selected examples of results from the variogram based analysis will be presented. Three types of images were examined. The first was an

ASTER image (15m resolution), the second a resampled Quickbird image so it mimics the resolution of the ASTER image, and the third a Quickbird image (2.4m resolution). As described ealier, the resampled Quickbird image was determined through a nearest-neighbor interpolation method, available as one of the standard functions with the Matlab software suite. Figure 3.6 to Figure 3.8 are the false colour composites of those images.

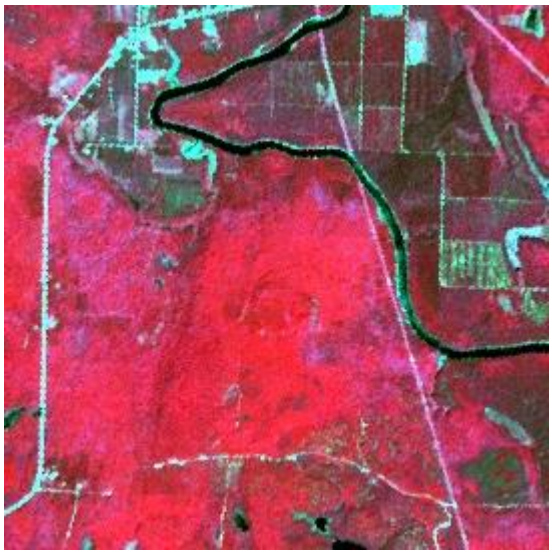

Figure 3.6. False colour composite of the ASTER study area. ASTER band 1 set blue, band 2 set as green, and band 3 set as red.

Figure 3.7. False colour composite of resampled Quickbird Image. Quickbird band 2 set to blue, band 3 set to green, band 4 red.

Figure 3.8. False colour composite of Quickbird Image. Quickbird band 2 set to blue, band 3 set to green, band 4 red.

Variogram analysis was applied to images from Figure 3.6 to Figure 3.8. Pixels which had an NDVI value below 0.05, were excluded in the analysis.

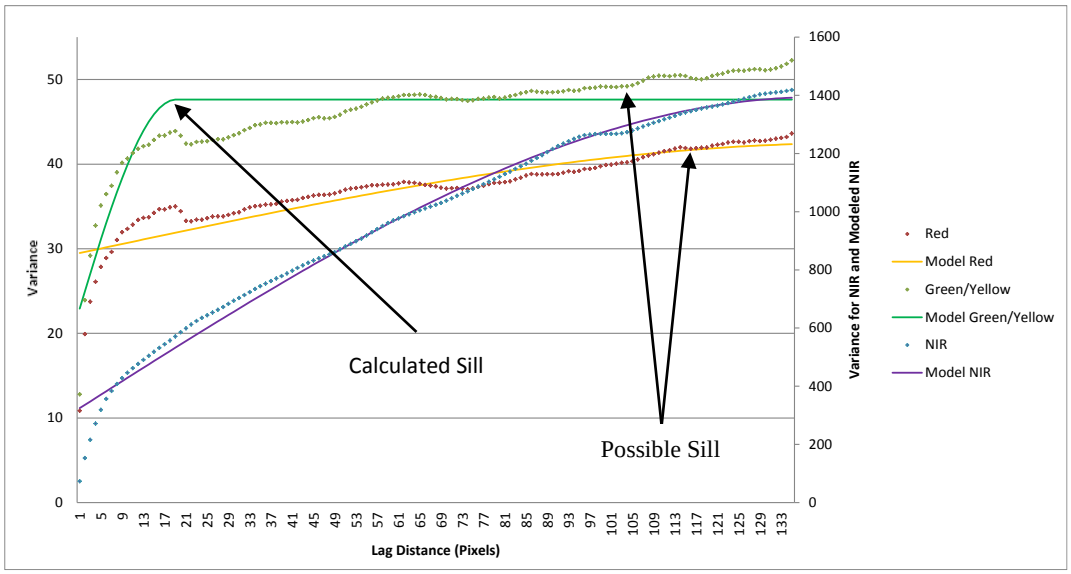

Figure 3.9. Plot illustrating all 4 measured variogram profiles and the corresponding modeled variogram determined from the ASTER image. Arrows indicating the location of the calculated sill for the modeled Green/Yellow band, and possible second sill location determined through visual inspection.

In Figure 3.9 for the NIR and Red bands, a sill location which was at the very end of the lag domain was produced due to the structure of the data and the sensitivity of the linear solver. A more logical sill location was determined for the

Green/Yellow band from the variogram. Through visual inspection a second possible sill location was also identified. This implies multi-scale features in the image.

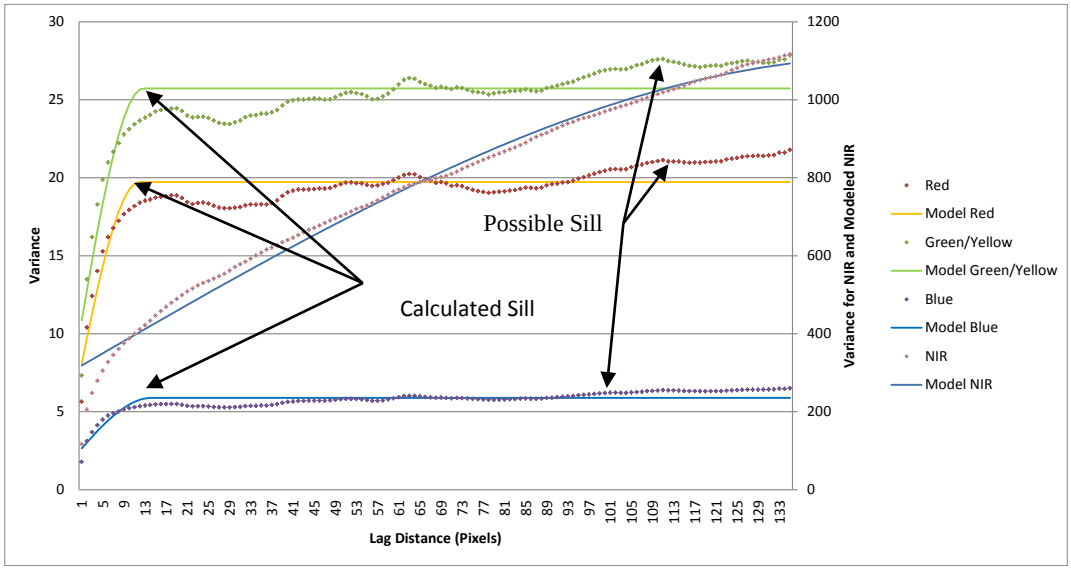

Figure 3.10. Plot illustrating all 4 measured variogram profiles and the corresponding modeled variogram profiles from the resampled Quickbird imagery. Arrows indicating the location of the calculated sill location and possible second sill location determined through visual inspection.

Unlike the ASTER imagery, the resampled Quickbird images produced logical sill values with the exception of the NIR band, which like the ASTER image, placed its sill value at the end of the lag domain. Also similar to the ASTER imagery a second

sill location was determined through visual inspection, again implying possible multi-scale features within the image.

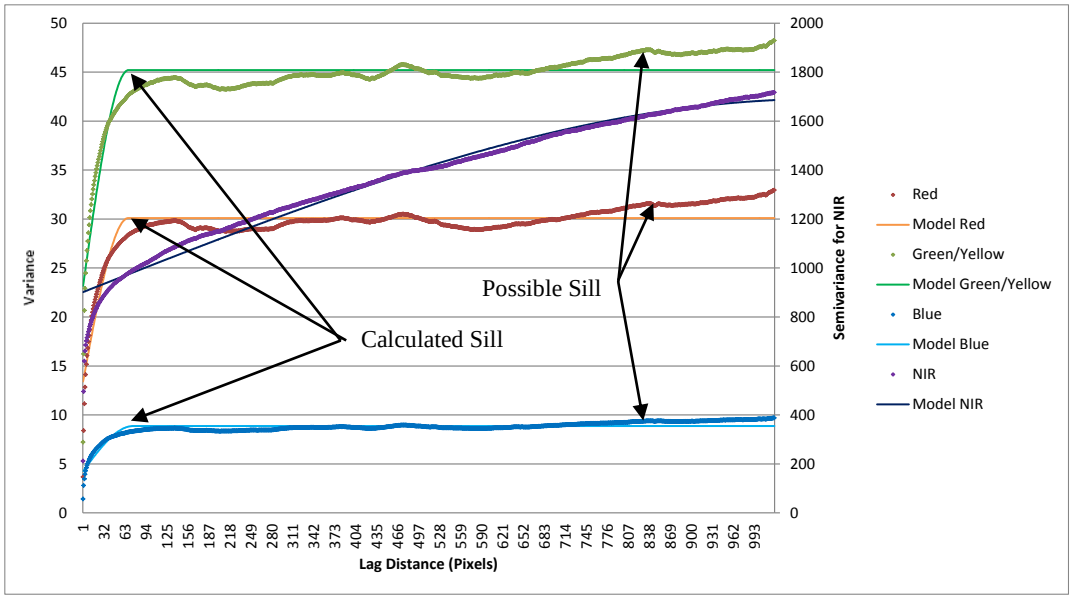

Figure 3.11. Plot illustrating all 4 measured variogram profiles and the corresponding modeled variogram profiles for the Quickbird imagery. Arrows indicating the location of the calculated sill location and possible second sill location located from visual inspection.

Similar to the resampled Quickbird images, the Quickbird images produced logical sill values with the exception of the NIR band which placed its sill value at the end of the lag domain. Also, similarly a possible second sill location was determined through visual inspection, which implies multi-scale features.

When utilizing the modeled values from Figure 3.9 to Figure 3.11 corresponding threshold values can be determined. When examining Figure 3.9 the sill values when averaged together yielded a value of 204, and a corresponding average lag value of approximately 20. The resampled Quickbird image yielded an overall sill value of 110 and a corresponding lag value of 12. When the definition of threshold described by (3.2) was used it yielded a possible threshold value of 4080 for the ASTER image. During initial testing a threshold value of 17500 was used to segment the ASTER and the resampled Quickbird image. This value was determined through user skill. This variogram determined threshold was approximately four times less than the actual value used to segment the ASTER image but it was useful in determine the 'neighborhood' of values to explore in order to determine a threshold which was done in subsequent testing. Examining the variogram results for the Quickbird image produced a scale value of 18620. Also, during initial segmentation testing of the Quickbird image, the threshold value used to segment the ASTER and resampled Quickbird image was 'scaled up', based on the difference in resolution, to approximately 109375, and used as the initial threshold value to segment the Quickbird image. To better understand how these threshold values fit in with the characteristics of the images, possible second sill locations were examined for all

images. These locations were determined through visual inspection, and another set of threshold values were determined. These second set of threshold values were 54316, 28776, and 358910, for the ASTER, resampled Quickbird and Quickbird image respectively. These results indicate that the discrepancy in threshold values between those determined from user skill and those strictly determined from variogram analysis can be explained by the multiple sill features present in the variograms based on image structures. These results indicate that a more complete approach to determining threshold values from variograms is a semiautomatic approach where user input is also used in order to determine the best threshold values based on multiple structures which may be present with the variograms. When implementing the first step in the adaptive image segmentation method each ASTER image has its variogram determined and a corresponding threshold value calculated from the methodology outlined above. After visual inspection if the threshold value appeared to be appropriate the ASTER image is then segmented and prepared for the next step.

3.4. BOUNDARY ADJUSTMENT METHOD

This section will provide the background on the boundary adjustment algorithm developed for this thesis. In order to adjust the boundaries of the ASTER determined, Quickbird projected segments, a concept based on applying energy-minimization to refining those segment boundaries was utilized. The proposed energy function uses the image gradient and local region statistics and an implementation strategy to carry out those adjustments. A physical analogy to how this method operates can be seen by considering the phenomenon of sand particles settling on a topographical feature. If a handful of sand is dropped on the top of randomly structured terrain. Under the influence of gravity, these particles would move to the most local area of minimum potential energy. This same principle of localized minimum potential energy is the inspiration behind the proposed boundary adjustment method.

3.4.1. THE ENERGY FUNCTION FOR BOUNDARY ADJUSTMENT

In this thesis, the energy function given in Equation (3.3) was designed in such a way that the following two goals were achieved: the adjusted boundaries were to be aligned well with the image features and additionally, the within-segment and between-segment variability was to be minimized and maximized, respectively.

$$\mathrm{E}_{i,j} = \sum_{k=1}^{N} \sum_{l=1}^{M_k} \frac{\sum_{m=1}^{B} \left(x_{k,l,m} - \mu_{k,m} \right)^2}{1 + w\left(\frac{y_{ij}}{y_{\max}} \right)} \tag{3.3}$$

In Equation (3.3) $E_{i,j}$ is the energy at the pixel (i,j) to which the initial boundary could possibly move; N is the number of segments; M_k is the number of pixels in the segment k; B is the number of bands in the image; $x_{k,l,m}$ is the digital number (intensity) of the pixel l in segment k for band m; $\mu_{k,m}$ is the mean value of the digital numbers for all pixels in segment l, for band m; y_{ij} is the value of pixel (i,j) in the

image gradient, for a particular adjustment scenario (described in further 3.4.4), and y_{max} is the maximum value in the image gradient for the entire image; and w is a weighting factor. In principle, w can take any positive value. Based on our experiments, when the value of w was up to 3-4, regional statistics had a limited effect on the energy function. In this study, to balance the contribution of image features and regional statistics to the calculated energy, w was fixed to 1. The effect of w on the boundary adjustments will be further analysed in the discussion and conclusions section. Initial segment boundaries were adjusted iteratively to new locations until a configuration was reached where E was at its local minimum within the pre-determined local neighbourhood.

3.4.2. BOUNDARY ADJUSTMENT

Given a high-spatial resolution image and initial segments obtained from a low-spatial resolution representation of the same scene, our method adjusted the segment boundaries by minimizing the energy function in Equation (3.3 according to the following four phases. In the first phase, called "Edge Mapping", the gradient (edge) image was created. In the second phase, called "Adjustment Calculation", for each

initial boundary location, all possible adjustments were determined and ranked according to the energy function in Equation (3.3) and the best adjustment scenario, in terms of the energy minimization, was recommended. In the third phase, called "Adjustment Ranking and Execution" the recommended adjustments in Phase 2 were ranked and executed, locally, in order of energy reduction. In the fourth and final phase called "Termination", oscillating adjustments and the termination criterion were checked. If the termination criterion was not met, Phases 2 to 4 were repeated. In the following sections, we will describe these phases.

3.4.3. PHASE 1: EDGE MAPPING

To generate a gradient component of the high spatial resolution image of interest, we implemented a canny edge detection algorithm [46] and applied it to the intensity component (grey-scale) of the test image, for each band *m*. With the implemented canny method, a Gaussian filter was first used to smooth the intensity image. The magnitude and the orientation of the gradient were then calculated using the Sobel templates. Finally, non-maxima suppression was used to remove any pixel that was not considered to be an edge. It should be noted, however, that the resulting image

was not binary; no threshold value was used. The resulting gradient images consisted of a range of values depending on the strength of that particular edge pixel. These images were then combined and averaged together to create a final gradient map, which was used to calculate the energy based on Equation (3.3) in Phase 2.

3.4.4. PHASE 2: ADJUSTMENT CALCULATION

The objective of this phase was to determine the possible movements of each boundary pixel. To do this, a circular buffer was projected around each candidate pixel. The candidate pixel belonged to the border of a segment called the base segment. The buffer encompassing the candidate pixel may often contain portions of the base segment and other segments. As an example in Figure 3.12 there are 3 different segments within the buffer around the candidate pixel B. For the base segment, there were six scenarios where its boundary could move from the candidate pixel B. As shown in Figure 3.13, the base segment could spread to a candidate pixel from one of the neighbours which could belong to other segments (Cases 1, 2, 3 and 4) or it could be shrunk by losing the candidate pixel to either of the other two

segments (Cases 5 and 6). The energy function defined in Equation 1 was calculated for each of these six possible adjustment cases and the original setting (Figure 3.12) with pixel (i,j) being at N4, N3, N2, N1, B, and B, respectively. To illustrate how to calculate the edge terms in Equation (3.3), it is assumed that the illustration in Figure 3.14 represents the locations of the edge pixels in this buffer. The blue squares represent edge pixels, and the thin red lines represent the boundaries of the buffer. These boundaries are identical to the boundaries of the buffer shown in Figure 3.12 and Figure 3.13. For each of the possible adjustment scenarios in Figure 3.15, a corresponding edge searching scheme was performed to determine the maximum edge magnitude, for that particular adjustment. As shown in Figure 3.15, for each potential adjustment scenario, pixels were checked along the direction of the adjustment (to the end of the buffer, illustrated by the gray pixels), and the maximum edge magnitude (y_{ij}) in that direction was selected for that particular adjustment. The adjustment scenario which provided the lowest energy was chosen as the recommended adjustment of the base segment at the candidate pixel. If none of the possible adjustments resulted in a lower energy, when compared to its present configuration, no adjustment was recommended. It should be stressed that no actual adjustments were performed in this phase. This process was repeated for all boundary pixels.

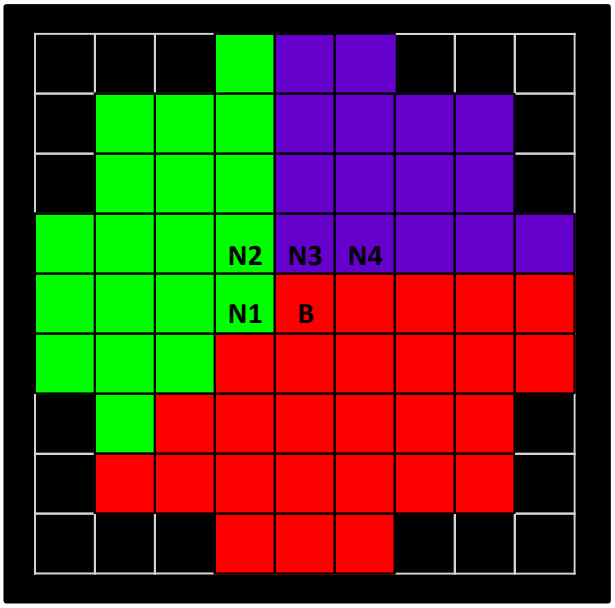

Figure 3.12. The buffer around the candidate pixel B illustrated through coloured pixels. There are three segments with red as the base segment. Note that the pixels in black are not part of the buffer.

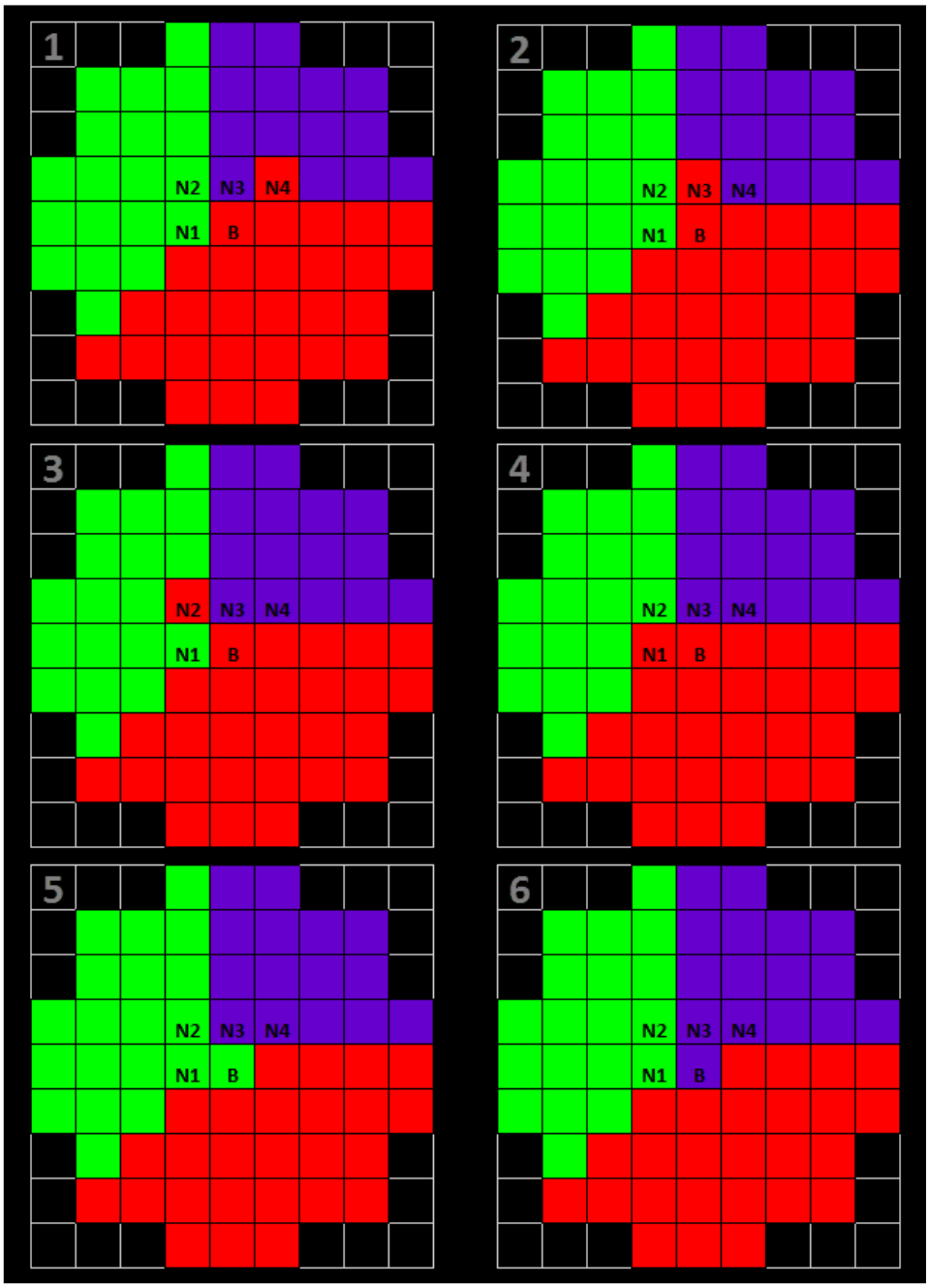

Figure 3.13. Six different adjustment scenarios, with their identification number, in which the boundary of the base segment (red) could move via the candidate pixel B.

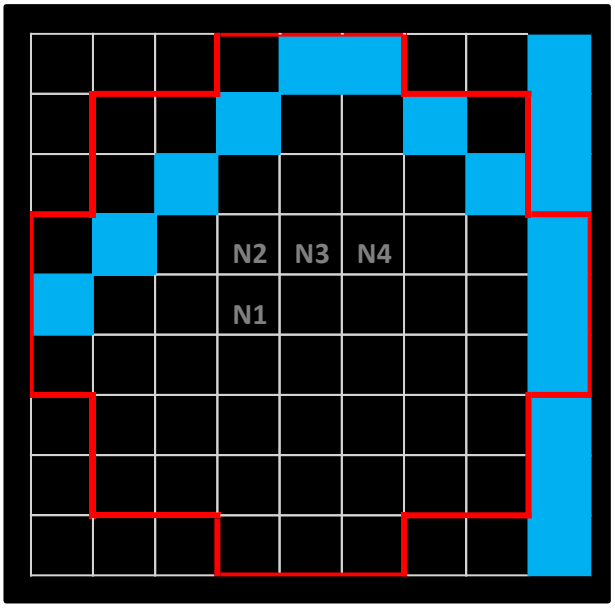

Figure 3.14. An example of the edge pixels (blue) in the buffer (red lines) around the candidate pixel B.

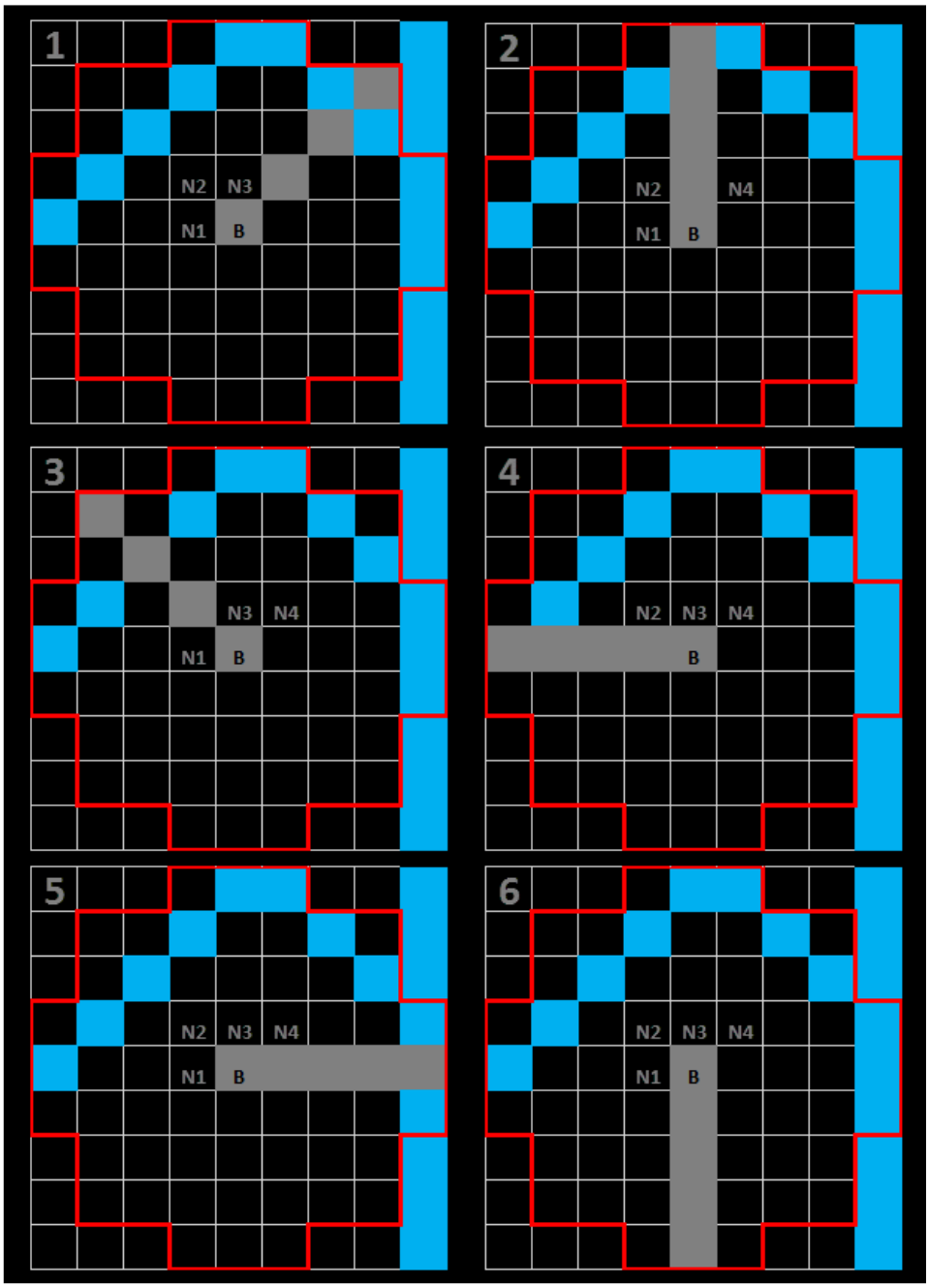

Figure 3.15. Searching schemes for the maximum edge magnitude for the six potential adjustment scenarios. The search direction is marked in gray.

3.4.5. PHASE 3: ADJUSTMENT RANKING AND EXECUTION

In this phase, the potential adjustments obtained in Phase 2 were ranked. This was carried out by first projecting a grid onto the high spatial resolution image overlaid with the initial segment boundaries. An illustration of the grids is shown in Figure 3.16. The recommended adjustments were ranked within each grid based on their minimization of the energy function from their previous configurations. The adjustment resulting in the maximum energy reduction, within that grid, was executed first followed by other adjustments based on their ranking of energy reduction. By doing so, adjustments were only affected by local features, and were carried out in a manner which rewarded the significance of the adjustment. Performing adjustments utilizing a grid was also advantageous because it produced groupings which are ideal for parallel computations. It is worth mentioning that oscillating adjustments were observed for some boundary pixels. An oscillating adjustment occurred when a boundary pixel was adjusted in one iteration, but was adjusted back to its previous positions on the next iteration; and this behaviour was repeated for subsequent iterations. This pixel oscillation was found to prevent the termination criteria from being met. To compensate for this, all adjustments were

tracked and if a pixel was identified to be oscillating, further adjustments were not allowed for that pixel.

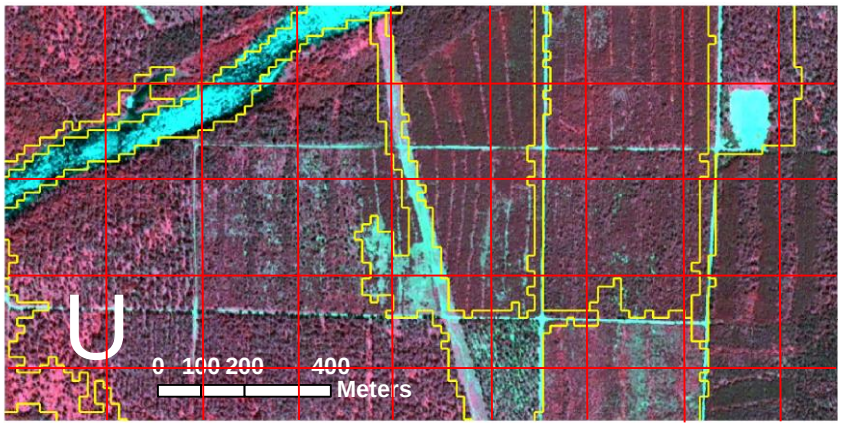

Figure 3.16. An illustration of the projected grid (red lines) used to group and rank adjustments. Potential adjustments obtained in Phase 2 were ranked within each grid before adjustments are carried out.

3.4.6. PHASE 4: TERMINATION

The termination criterion was checked in this phase. The termination criterion was defined as the point when the number of adjustments, per-iteration, reached below a user specified level or zero. Also, termination of the algorithm was carried out if the maximum number of iterations, specified by the user, was reached. If the termination criterion was not met, Phases 2 to 4 were performed again.

3.5. FINAL SEGMENTATION OF QUICKBIRD IMAGERY

The variogram based threshold determining method described in 3.3 was applied to the areas of the images outlined within each adjusted segment from the Quickbird image. Once determined each individual, adjusted, segment was further segmented based on these threshold values. Based on these results if parts of the image appeared to be either undersegmented or oversegmented the threshold values, and their corresponding vaiograms were further examined and if needed further adjustments to the threshold values were done and the image was resegmented. If these results were satisfactory the image was considered to be successfully segmented. It should be noted that provisions are in place with this version of the methodology to mask out areas which are primarily water, to exclude them from segmentation. However, this feature was not activated for these test for simplicity of testing. In future iterations individual segments will also be examined, automatically, and determined if further segmentation is required. If further segmentation is not necessary these segments will not be further segmented.

Chapter 4

RESULTS

In this section results from individual methods and from the entire flow of the developed segmentation methodology will be presented. In the first section results illustrating outputs from the region growing program will be shown to illustrate its functionality. Next results from the boundary adjustment method will be presented. These results will show how the boundary adjustment method is affected by different image features and the varying levels of quality which can be achieved. Finally, this chapter will end with a section showing the entire segmentation process using the developed methodology.

4.1. SEGMENTATION RESULTS

This section will present segmentation results to illustrate the functionality of the developed image segmentation program. The first set of results are produced from an ASTER image, which was segmented using two sets of parameters. These tests were used to verify that as threshold values changed the resulting segmentation map produced result which were consistent with expected structures and changes.

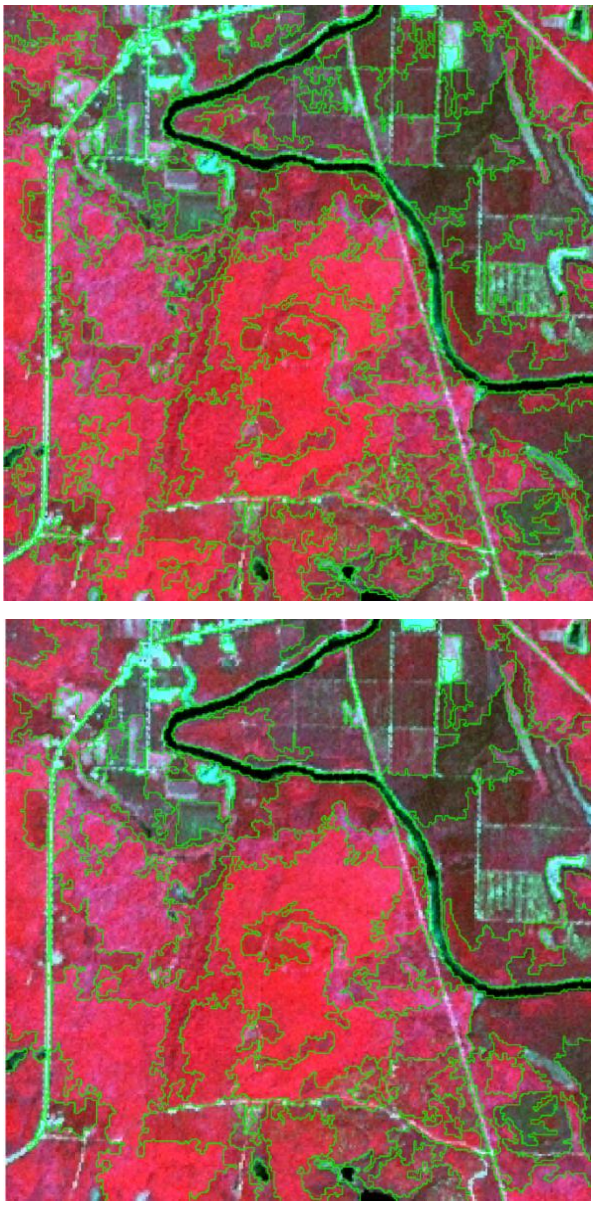

Figure 4.1. Top, ASTER image segmented with scale value of 4080. Bottom, ASTER image segmented with scale value of 15400.

The segmentation threshold values used to produce the results in Figure 4.1 were determined using variogram analysis. The value of 4080 was determined from the first sill location and 15400 from the second sill location from the variogram of the image. When interpreting Figure 4.1 it was noted that when the threshold value was increased the number of segments was reduced. Also, when comparing the segmented map of the lower threshold to the higher thresholded one, small segments present the lower threshold map should not be present on the higher threshold map, while preserving the structure of the larger segments which remain. The merging of the smaller segments should not affect the structure of the larger segments. In Figure 4.1 these features were present.

4.2. BOUNDARY ADJUSTMENT RESULTS

In this section results produced using the boundary adjustment algorithm (described in chapter 3.4.2) are presented. Results of adjustments from both a U-shaped test object and from a remotely sensed imaged will be shown. The segment boundaries shown in Figure 4.3, Figure 4.5, and Figure 4.6 were adjusted. The U-shaped test

object acts as a basic test image in order to evaluate the performance of the method with a simple structured image. A 5 by 5 Gaussian filter was used to smooth the image as part of an edge detection method (Phase 1) and the result is shown in Figure 4.2 and Figure 4.3. A buffer with a radius of 10 pixels was used in Phase 2 to determine all of the possible adjustment scenarios for each of the initial boundary locations. A grid size of 20 by 20 pixels was used in Phase 3 to rank the potential adjustments and the termination criterion was set when adjustments reached below 1 adjustments per iteration, with the maximum number of iterations limited to 120. The selection of these parameters will be discussed later. The final adjusted-segments are shown in Figure 4.4, Figure 4.5 and Figure 4.6. Comparing with the original projected boundaries, the adjusted boundaries are smoother and align well with image features. In particular with the U-shaped object where the test boundary has been clearly adjusted to the features of the U-shaped object. To clearly show the difference between them, several close-up images are shown in Figure 4.7 and Figure 4.8. For these close-up areas the initial projected segments can clearly be seen to not match the boundaries of the features in the image. However after adjustment, those same segments show improvements in both their location and neatness, when compared against those same image features. These adjusted

boundaries are very close to easily identified edges and encompass easily identifiable homogeneous areas.

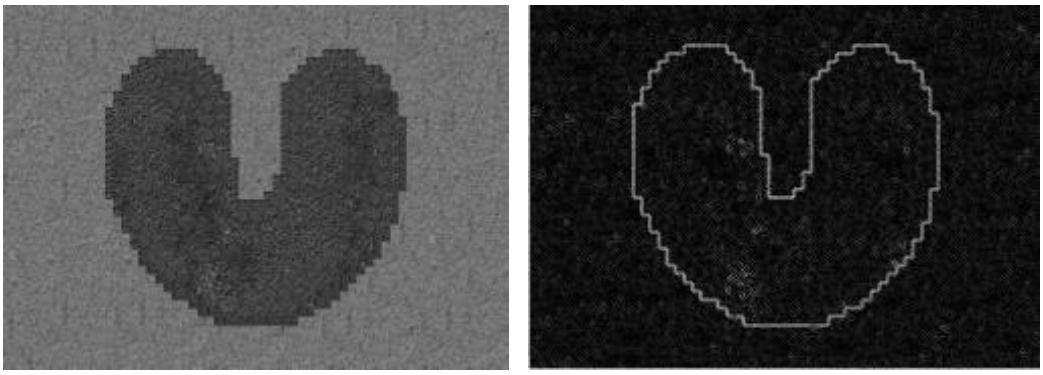

Figure 4.2. Intensity map of the U-Shaped Object image (left) and its corresponding gradient map (right).

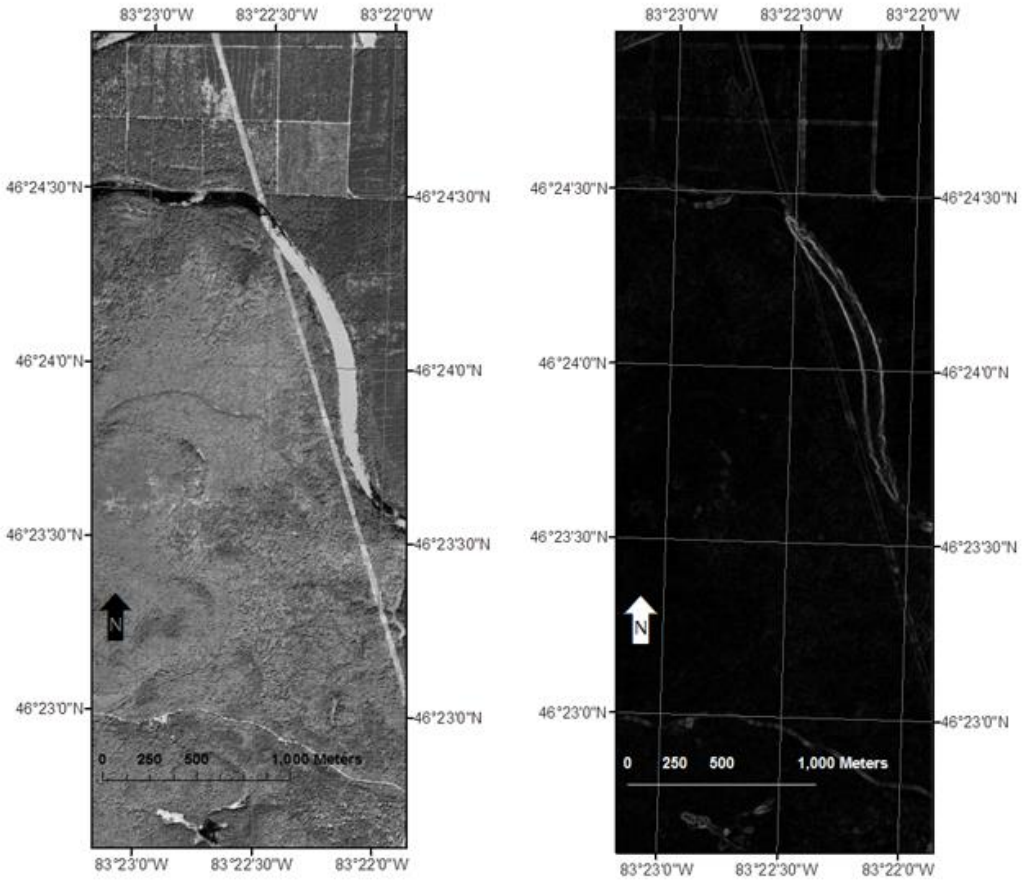

Figure 4.3. Intensity map of the Quickbird image (left) and its corresponding gradient map (right).

Test Boundary

Before Adjustment

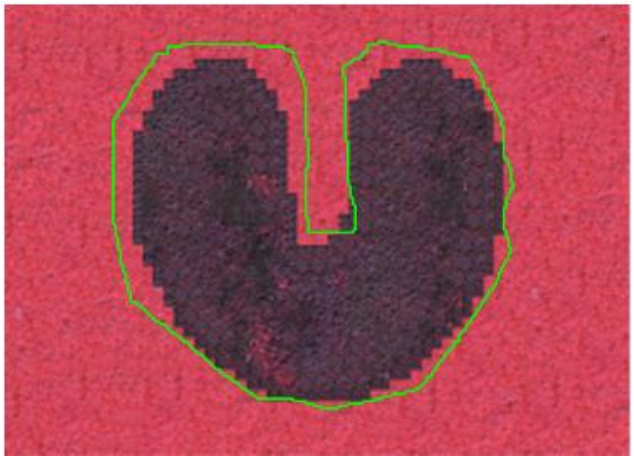

After Adjustment

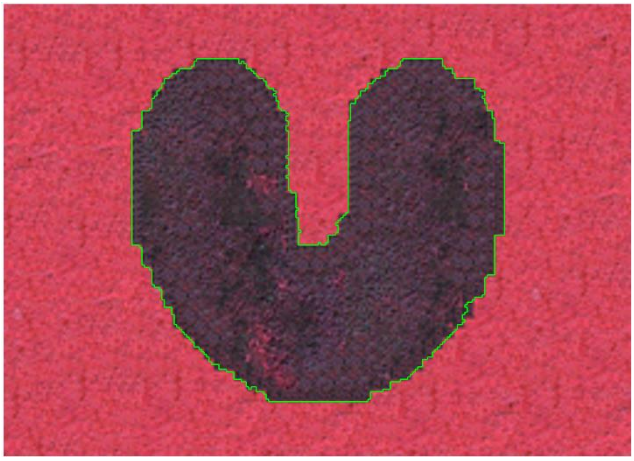

Figure 4.4. The test boundaries for the U-Shaped object (top) and their corresponding adjusted segments (bottom).

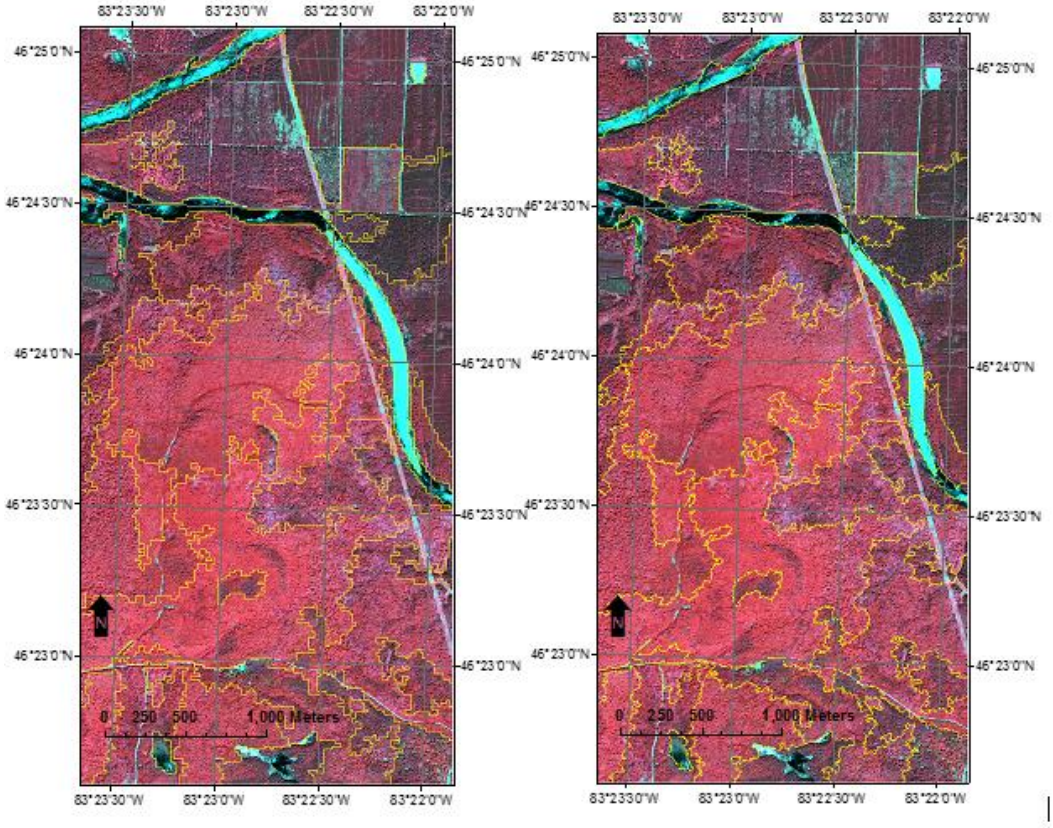

Figure 4.5. The boundaries of the initial segments determined from the resampled Quickbird image (left) and adjusted-segments projected onto the Quickbird image (right).

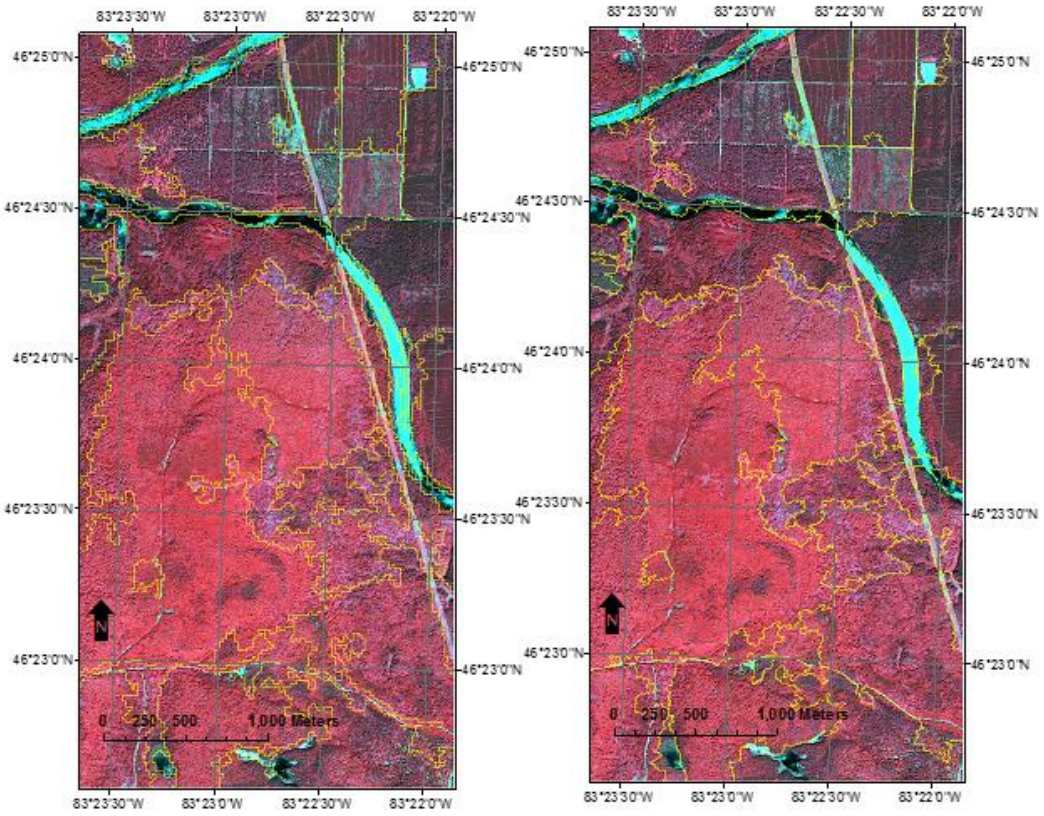

Figure 4.6. The boundaries of the initial segments determined from the ASTER image (left) and adjusted-segments projected onto the Quickbird image (right).

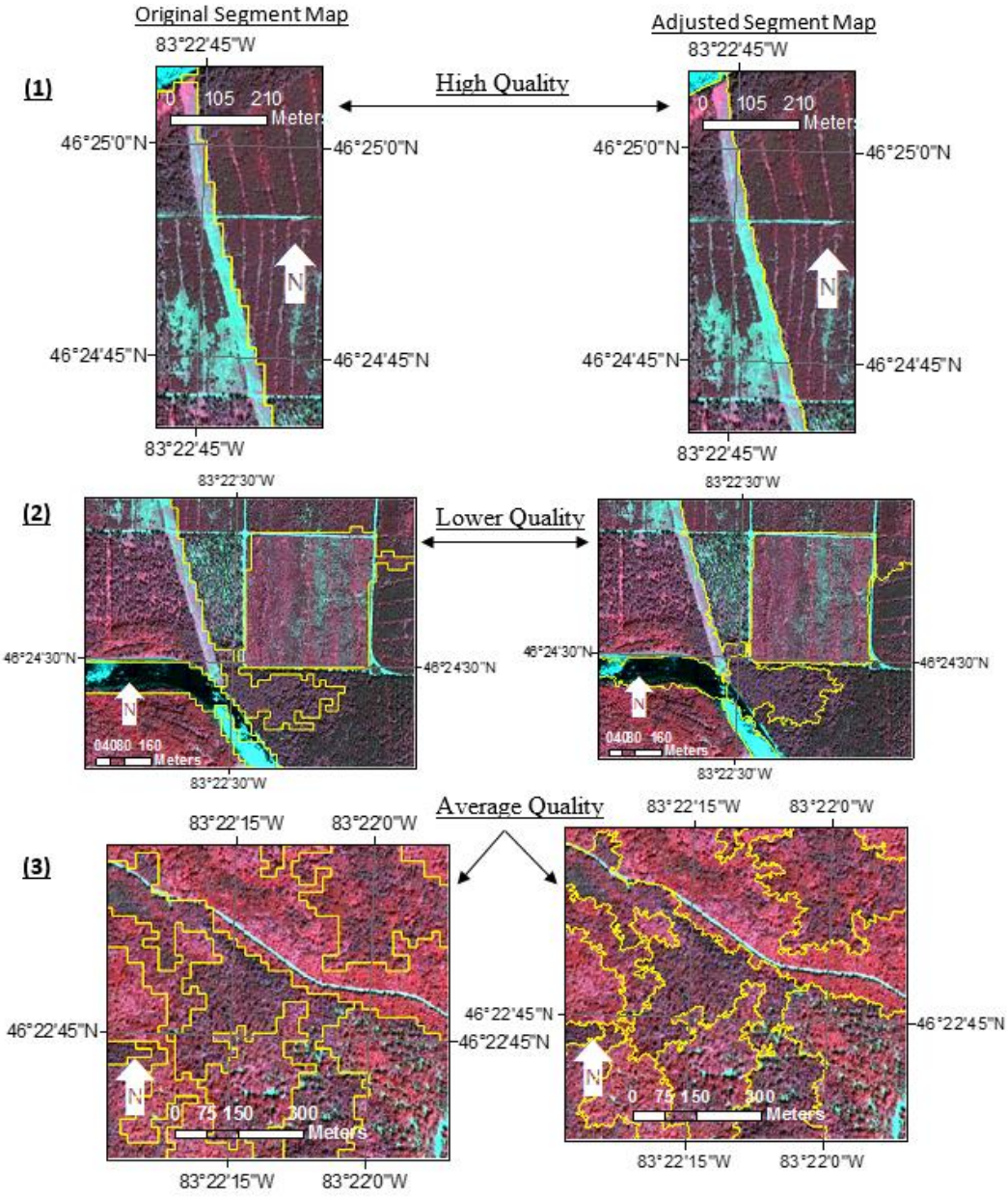

Figure 4.7. Projected segments determined from the resampled Quickbird image (left) and adjusted-segments (right), for areas 1 to 3. The quality of the adjusted result was classified using a three level (high, average, lower) classification scheme further explained in 5.1.

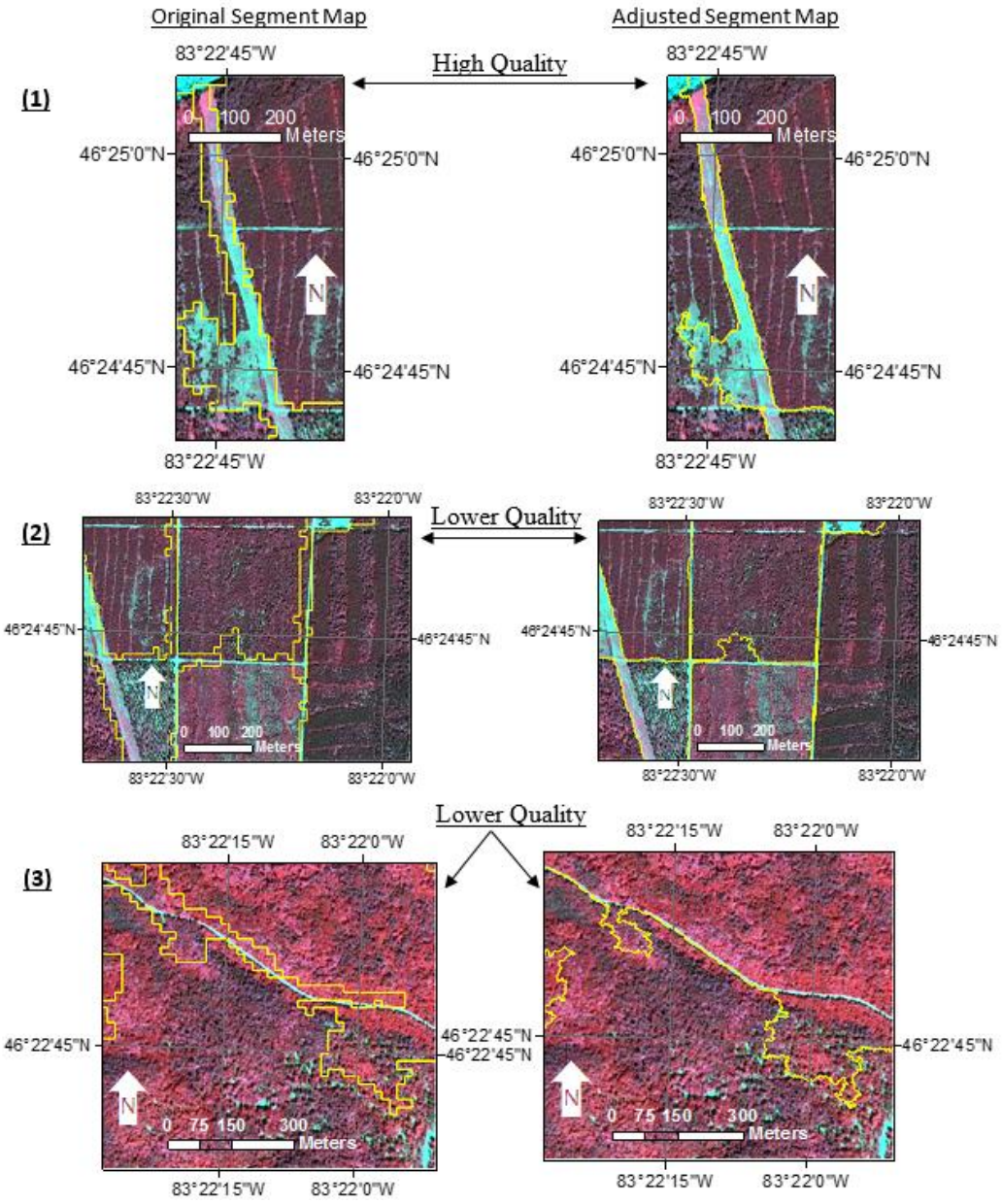

Figure 4.8. Projected segments determined from the ASTER image (left) and adjusted-segments (right), for areas 1 to 3. The quality of the adjusted result was classified using a three level (high, average, lower) classification scheme further explained in 5.1.

4.3. ADAPTIVE SEGMENTATION RESULTS

In this section we will present results of the adaptive segmentation method. To test the developed method, two areas from the test image shown in Figure 3.1 were selected. These test areas represented an area of approximately 400 by 500 pixels, on the high resolution image. These areas were selected because they contained various land cover types and were of a large enough area to contain multiple segments from the low resolution representation on the image, and yet small enough that when projected onto the corresponding high resolution image that it could be easily analyzed within a reasonable amount of time. For these tests the low resolution image utilized was an ASTER image and the high resolution image was Quickbird sourced imagery, from the same study area used in Figure 3.1. In Figure 4.9 the test areas are indicated on the high resolution Quickbird image.

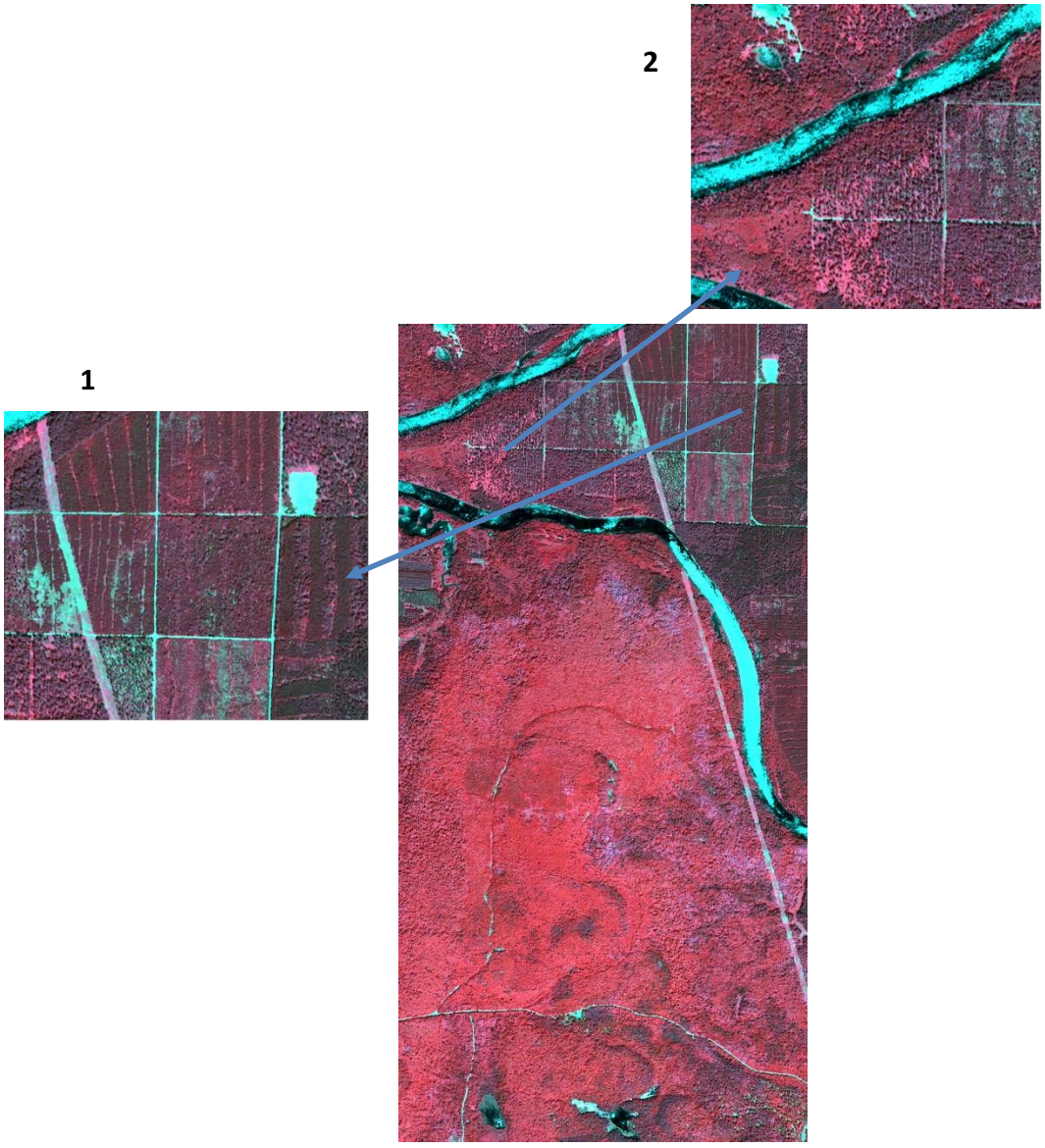

Figure 4.9. Illustration of the test areas which are to be segmented by the proposed segmentation method.

In order to complete the segmentation process, and to remain consistent with results shown in 4.2, the ASTER image was segmented using the same threshold value, and adjustments were performed with a buffer with a radius of 10 pixels, and a gird size of 20 by 20 pixels. A 5 by 5 Gaussian filter was used to smooth the image in order to create the edge map, and adjustments were terminated when adjustments reached 1 per iteration. Figure 4.10 and Figure 4.11 shows the initial segmentation process where the low resolution imagery was segmented and then projected onto its corresponding high resolution imagery. Figure 4.12 and Figure 4.13, show the end result where the adjustment process has been completed and the individual projected, adjusted, segmented map has been further segmented using the region growing program, with scale values determined by the variogram based method. Before segmentation, each variogram determined scale value was examined, along with its accompanying variogram, to determine if they corresponded well with one another. If not, they were manually adjusted. Once all scale values were determined to be satisfactory, segmentation was executed.

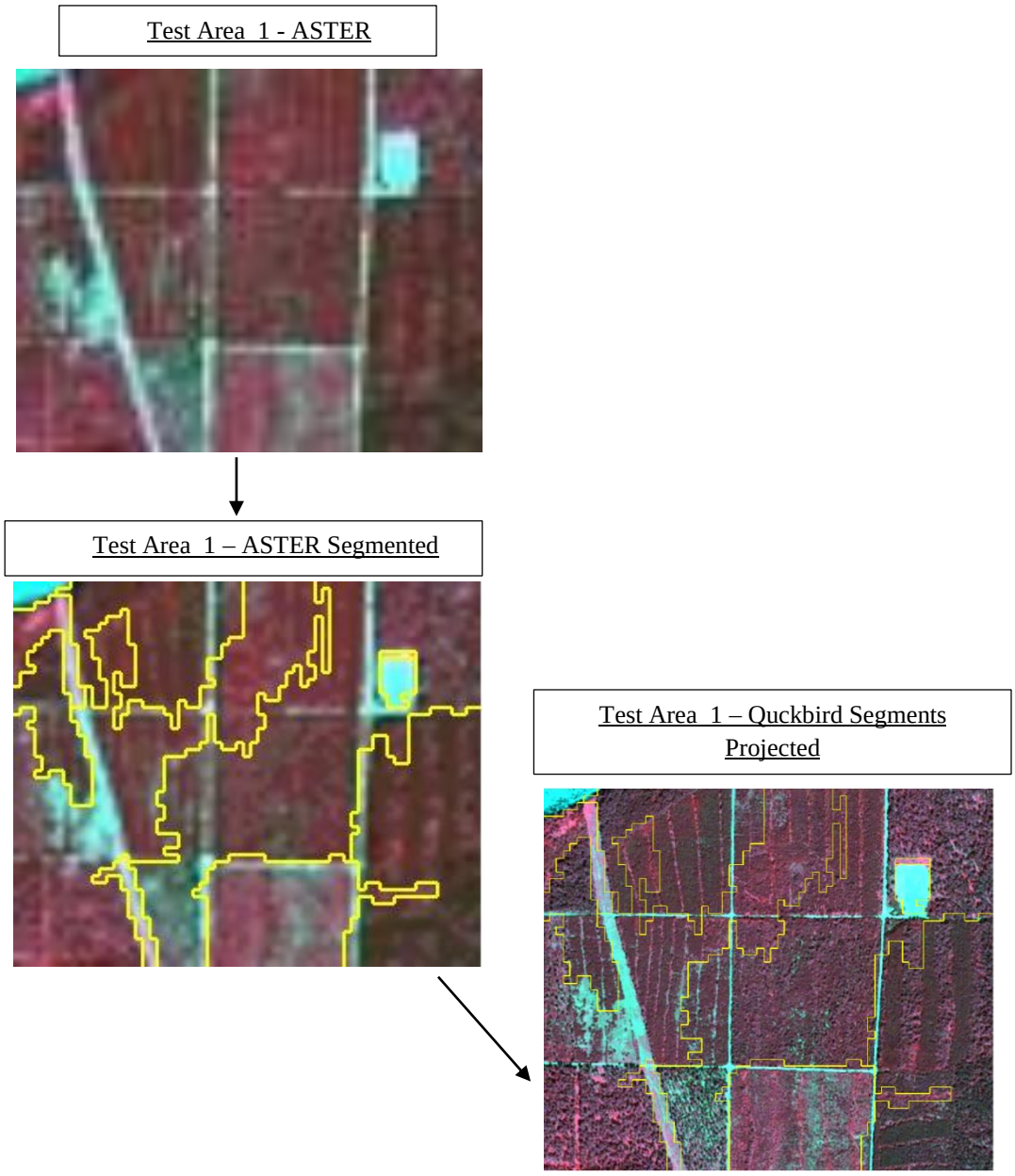

Figure 4.10. Illustration of Test area 1's original segmentation and projection onto its corresponding high resolution image.

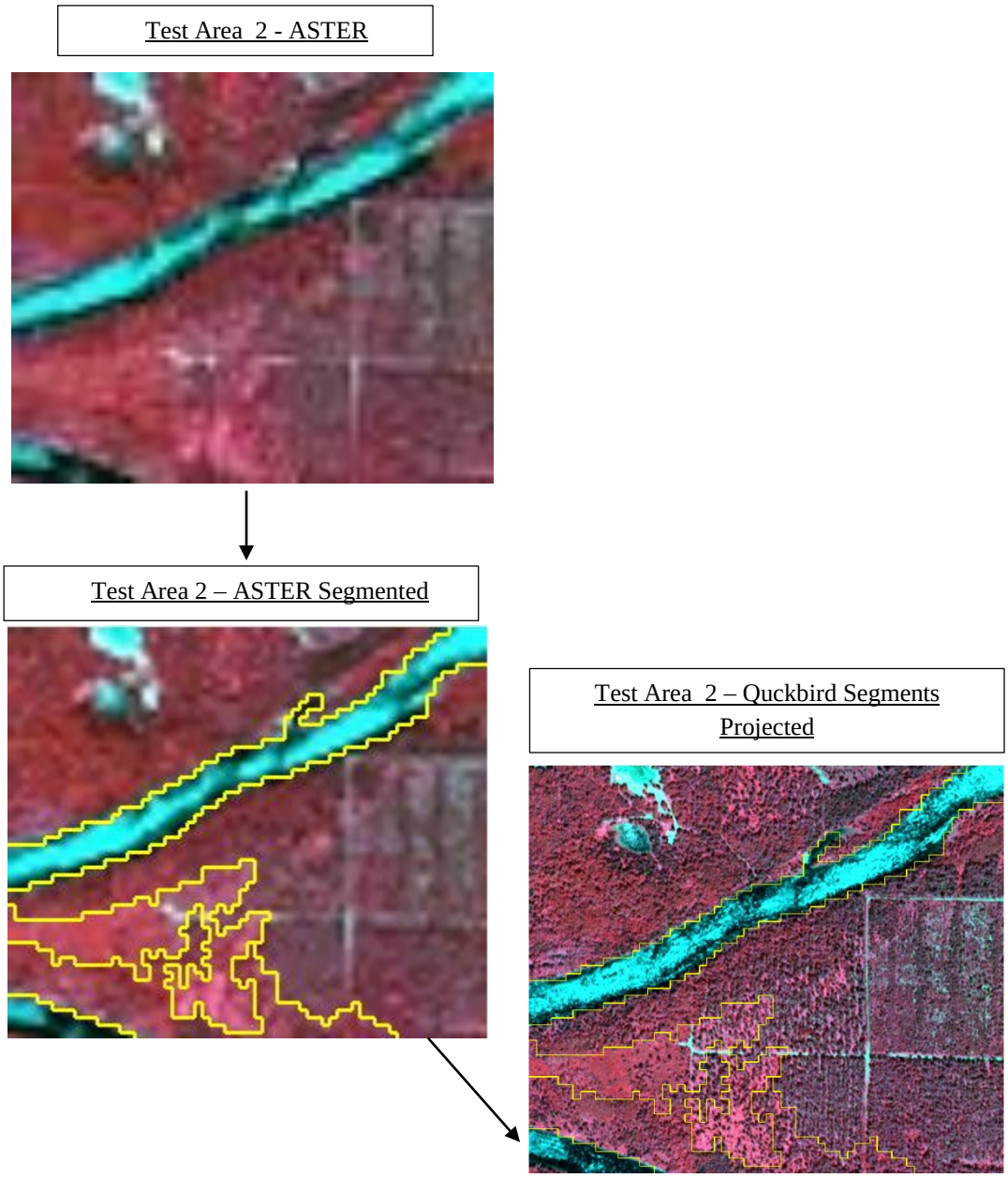

Figure 4.11. Illustration of Test area 4's original segmentation and projection onto its corresponding high resolution image.

Test Area 1 – Segments Adjusted

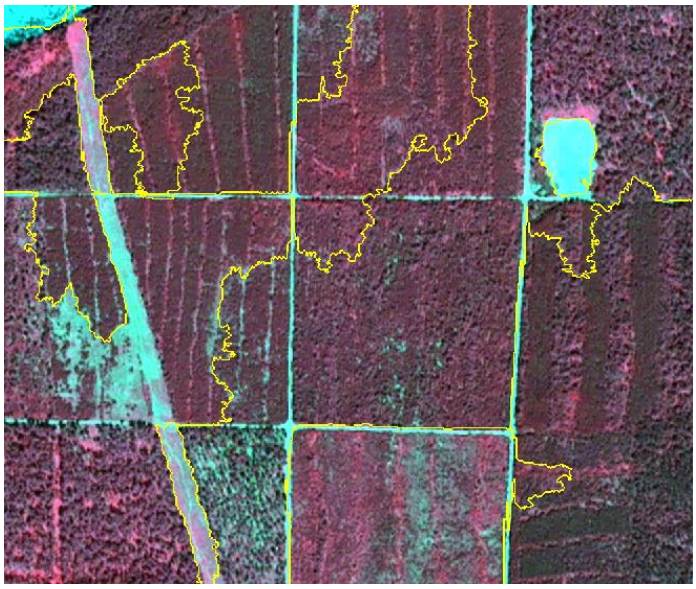

Test Area 1 – Final Segments

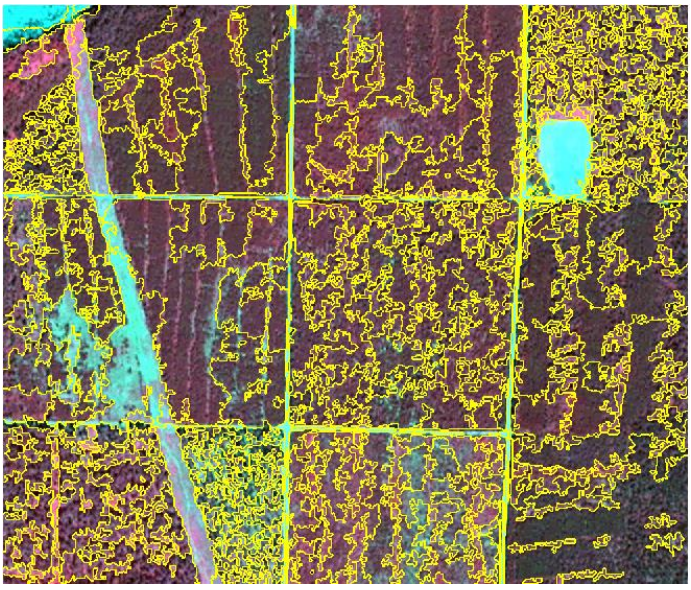

Figure 4.12. Test area 1 showing its projected segments, now adjusted (top), and the final segmented result (bottom).

Test Area 2 – Segments Adjusted

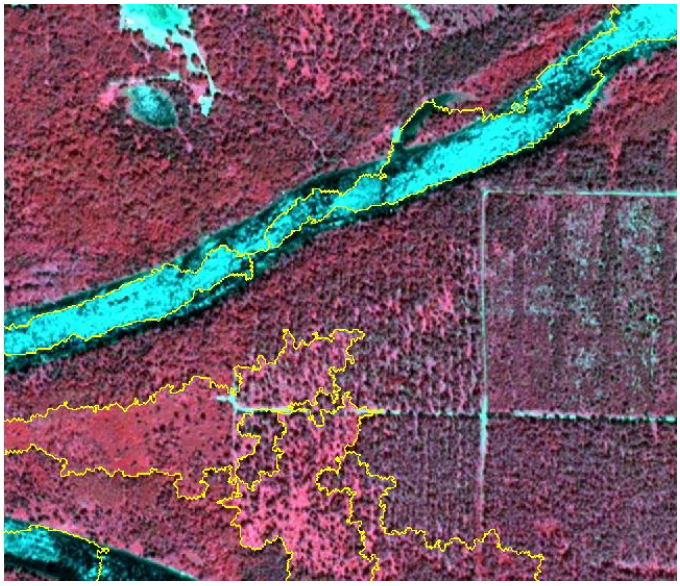

Test Area 2 – Final Segments

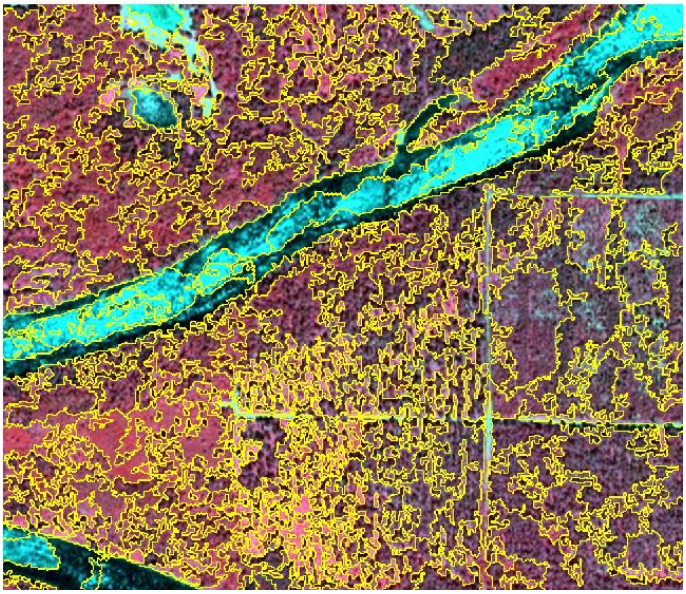

Figure 4.13. Test area 2 showing its projected segments, now adjusted (top), and the final segmented result (bottom).

Chapter 5

EVALUATIONS

In this chapter evaluations of the results presented in Chapter 4 will be discussed. It will consist of two sections. The first section will cover the results from the boundary adjustment method presented in 4.2 and the second section will cover the adaptive segmentation results presented in 4.3.

5.1. EVALUATION OF BOUNDARY ADJUSTMENT RESULTS

Several quantitative measures and one qualitative measure were used to explore the quality of the adjusted results. The first quantitative measure compared the

homogeneity, as measured by changes in the standard deviation of the segments before and after adjustment and the second quantitative measure was done through the adjusted segments F-measure score. The qualitative measure was a three level classification approach which was determined through user input.

As a note on F-measure score, F-measure score was selected as the main means for quantifying the evaluation of the adjustment method for several reasons. It is a standard method which is used by a number of studies and the basis of evaluation of the Berkley image segmentation benchmark dataset, which is considered to be a valuable resource in comparisons of image segmentation algorithms [13,16]. Furthermore, F-measure is easy to implement and does not require a negative case for comparison. It simply requires a single positive case for comparison, which in this case is the human generated map.

After adjustment segments were found to be more homogeneous, as demonstrated by a decrease in the segments average standard deviation values, determined from the red, green and near-infrared bands from the adjusted-segmented Quickbird image. When the average standard deviation was calculated and compared, based on

all segments, before and after adjustment, shown in Table 3 A and B, a decrease in the standard deviation was observed, indicating improved homogeneity. These changes were especially evident with segments determined from the resampled Quickbird image. Adjustments performed on segments determined from the resampled Quickbird image, for the majority of tests, outperformed segments determined from the ASTER image, both in terms of visual inspection and in measured changes in homogeneity. The next evaluation method which was used was qualitative. This qualitative measure is a three level quality classification scheme determined by user input. Through this classification scheme adjusted results were either classified as being of high, average or lower quality. When comparing quality classification results from Figure 4.7 and Figure 4.8, it should be noted that two of the adjusted results from the ASTER image were deemed to be of lower quality (areas 2 and 3), with one being high quality (area 1). For areas 2 and 3 from the resampled Quickbird image only area 2 was deemed to be of lower quality, while area 3 was determined to be of average quality, and area 1 was determined to be a high quality result. These results tied in with better overall homogeneity changes, summarized in Table 3A and B, implies that the adjustment method may perform better on segments determined from a resampled Quickbird image, compared to segments determined from an ASTER image, of the same area. It is speculated that

this was caused due in part from consistency in collection dates for the imagery, and consistency between sensors. These consistencies resulted in the resampled Quickbird image producing results which outperformed results from the ASTER imagery.

(A)

Test Boundaries for **U-Shaped Object**	Average standard deviation		
	Red	Green	Near-infrared
Before adjustment *(Test Boundary)*	5.683	3.044	3.56
After adjustment *(Test Boundary)*	3.983	2.914	3.390

(B)

Initial Segments Determined from **Resampled Quickbird**	Average standard deviation		
	Green	Red	Near-infrared
Before adjustment	3.328	2.255	19.547
After adjustment	2.774	1.863	16.721

(C)

Initial Segments Determined from **ASTER**	Average standard deviation		
	Green	Red	Near-infrared
Before adjustment	5.718	4.595	22.197
After adjustment	4.466	3.749	17.803

Table 3. Average standard deviation of the digital numbers (intensity) in the green, red, and near-infrared bands, before and after adjustment, for segments from the Quickbird image. Values are calculated by averaging all segments, for each band. Initial segments determined from the U-shaped Object (A), resampled Quickbird image (B) and from the ASTER image (C).

The second quantitative analysis method, in the form of F-measure, was applied to the adjusted segment maps shown in Figure 4.7 and Figure 4.8, using a window of radiuses between 3-5 pixels, which are standard window distances for images of these sizes [47,48]. Those results are summarized in Table 3. When examining Table 3 it is noted that as the window size to match pixels increases as does the F-measure values. Furthermore it was noted that all adjustments resulted in improved F-measure values, and were performing either at or above a threshold of 0.58-0.66 which corresponds to F-measure values generated by the best results from widely used image segmentation and adjustment algorithms [47,48], and in some cases performing at the level between 0.79-0.84 which was generated from human determined segmentation or adjustment maps which are compared to one another. These results indicate that the proposed method was functioning as designed and was producing adjustments which match closely to those which would be created by other methodologies or human perceptions.

(A)

F-measure Determined from test areas **before adjustment**	Window Size(pixels)		
	Radius = 3	Radius = 4	Radius = 5
ASTER Area 1	0.243	0.324	0.399
ASTER Area 2	0.164	0.219	0.269
ASTER Area 3	0.170	0.226	0.279
Resampled Area 1	0.240	0.320	0.394
Resampled Area 2	0.209	0.278	0.342
Resampled Area 3	0.168	0.224	0.278

(B)

F-measure Determined from test areas **after adjustment**	Window Size(pixels)		
	Radius = 3	Radius = 4	Radius = 5
ASTER Area 1	0.882	0.895	0.895
ASTER Area 2	0.571	0.595	0.604
ASTER Area 3	0.578	0.604	0.625
Resampled Area 1	0.862	0.876	0.883
Resampled Area 2	0.707	0.743	0.768
Resampled Area 3	0.567	0.594	0.620

Table 4. F-measure calculated for adjusted segments for window radiuses between 3 to 5 pixels before adjustment (A), and after adjustment (B).

5.2. EVALUATION OF ADAPTIVE SEGMENTATION METHOD

In order to evaluate the performance of the adaptive segmentation method, the results were compared to segmentation results which were produced by a single set of parameters, illustrated in Figure 5.1 and Figure 5.2.

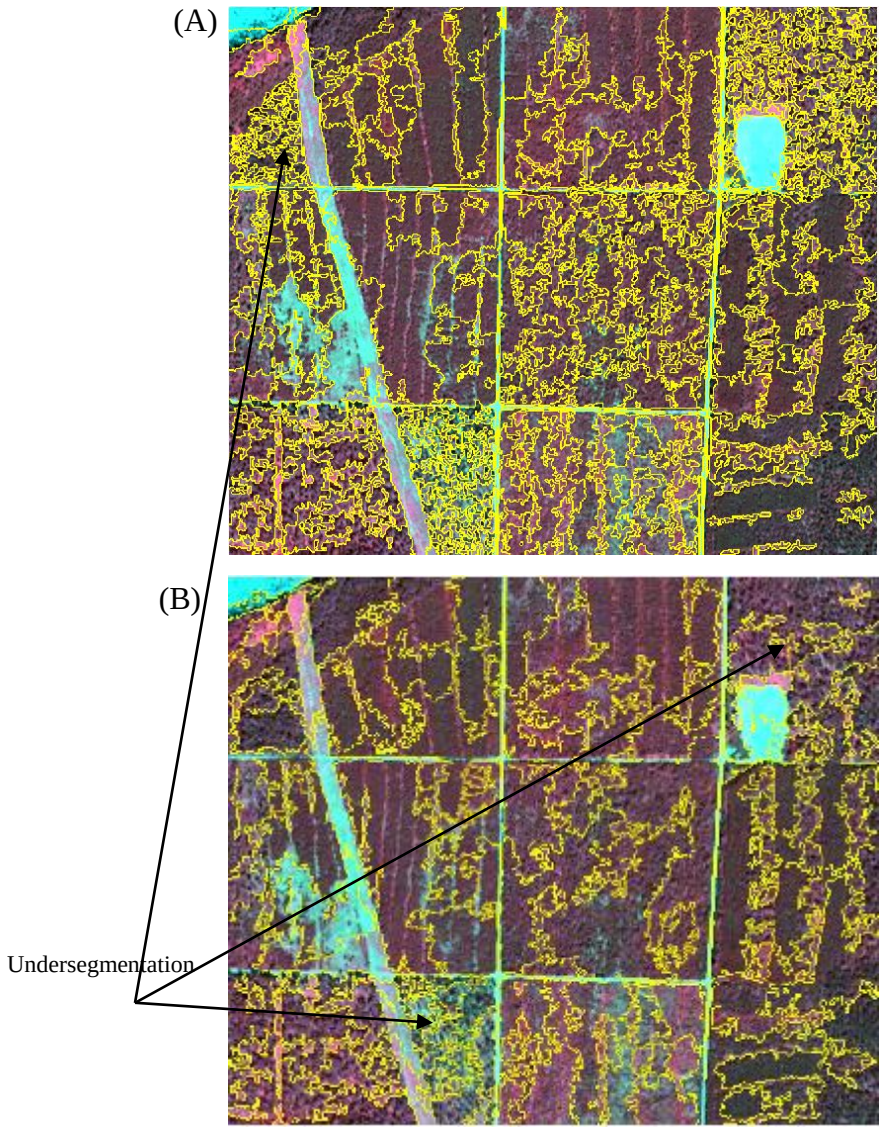

Figure 5.1. Test area 1, when segmented using the adaptive method (A) and test area 1 segmented using a single set of parameters (B).

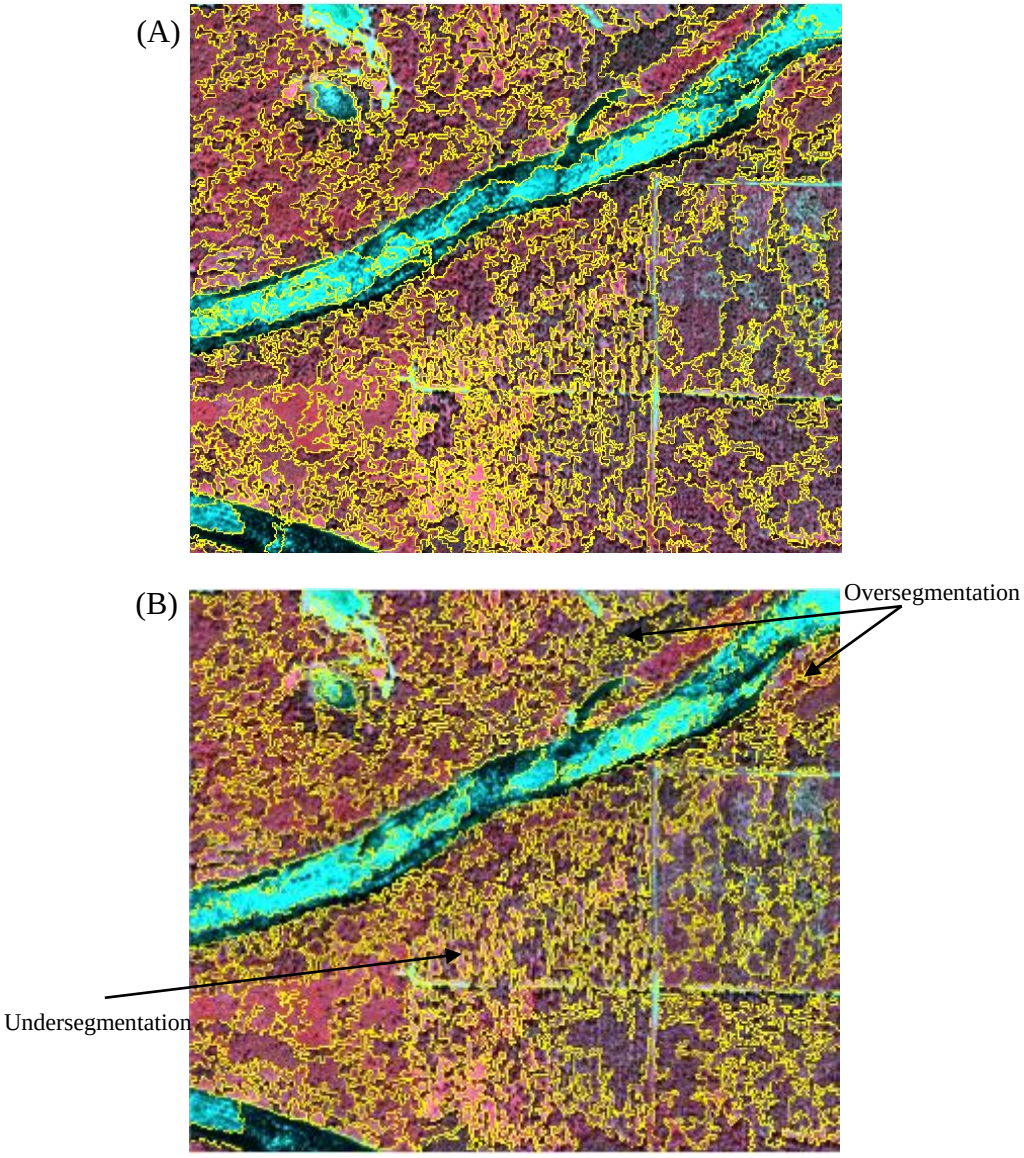

Figure 5.2. Test area 2 when segmented using the adaptive method (A) and test area 2 segmented using a single set of parameters (B).

The parameters used to create the single parameter segmentation results were determined by analyzing the entire test image using the variogram based method. These results show under segmentation in many areas when compared to the adaptive results. In areas of complex cover the adaptive results produced more segments while not over segmenting less complex areas. Also, with the case illustrated in Figure 5.2 some areas defined by in Figure 5.2 (B) were over segmented. These results indicate that the adaptive segmentation method was working as designed.

Chapter 6

DISCUSSIONS AND CONCLUSIONS

This chapter contains the discussion and conclusions for the thesis and will end with a section on looking ahead and future work. The discussion and conclusions will begin by focusing on results produced by the boundary adjustment method and end with results from the adaptive segmentation method. The final section will examine future plans for both the boundary adjustment method and the adaptive segmentation method and how these methods fit into a grander strategy for the research this group wishes to accomplish.

6.1. DISCUSSION

When examining the results of the proposed adjustment methodology, we first considered the U-Shaped test image. Upon visual inspection it can be clearly seen that the test boundary has been significantly adjusted, and the adjusted boundary matches well to the U-Shaped objects features. From the first quantitative measure of improved homogeneity, as measured by a decrease in standard deviation, averaged from all segments after adjustment implies that the adjustment methodology was working as designed. Further quantitative analysis in the form of F-measure also supports this with high F-measure values. These visual and quantitative results indicate that the proposed adjustment methodology was functioning as designed. For boundary adjustment or segmentation methods whose performance was measured through F-measure values, it was generally agreed upon that segmentation or adjustment results which produce F-measure values between 0.79-0.84 and above are comparable to those generated when human generated maps are compared to one another [47,50,51]. According to these F-measure results testing of the U-Shaped object indicate that our proposed methodology was generating results which would be comparable to other methods and those generated by human perceptions. It should be stressed however, that the focus of this thesis

was not a comprehensive comparison of the developed methodology to other active contour or boundary adjustment methods but a successful application of it with remotely sensed imagery.

When examining the results of the boundary adjustment method, we also considered the size and complexity of the test image. The test image was fairly large (1934 by 967 pixels) with over 50 individual segments comprising over 30,000 boundary pixels. Additionally, the image was complex, containing many different types of terrain, which adds value to our testing. Related to this, due to the size and complexity of the test image it was deemed unreasonable to create a manually determined segment map for all of the adjusted boundaries for comparison purposes, an example is shown in Figure 6.1.

Segments Before Adjustment

Human Determined Adjustments

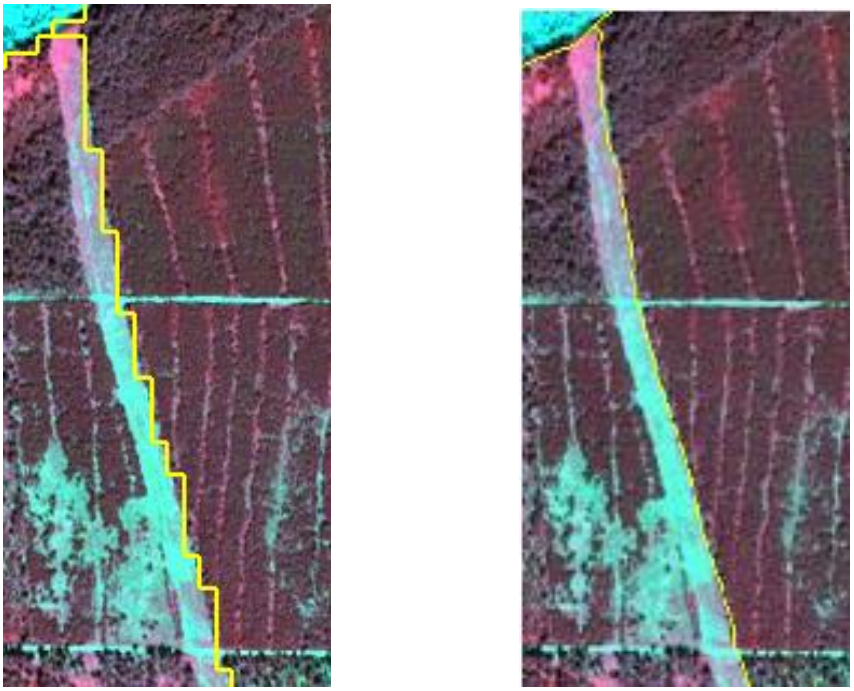

Figure 6.1. Example of segment map before adjustment (left) and adjusted segment map determined through human perceptions (right) for use in quantitative evaluations.

Ideally, we would manually adjust the segment boundaries to generate reference segments, to act as references for quantitative evaluation. Such an evaluation was employed for a small study site in a separate study. [49]. Instead, individual test areas for further examination were chosen and independent evaluators from our

group and from a conference, were allowed to examine our results, who then helped to create adjusted segment maps for the test areas, which are highlighted in Figure 4.7 and Figure 4.8, and also aided in ranking those adjustments based on the quality. By the initial quantitative measure, improved homogeneity as measured through decreases in standard deviation values of the segments, after adjustment, supports our assertion that our method was successfully adjusting results. When analysis using F-measure values was conducted, it was noted that even with a window of 3 pixels adjusted segments, from the selected test areas, produced F-measure values which were improvements from their original scores and were close to or at the levels of those produced by other methodologies and in the case of test area 1, for both the ASTER and resampled Quickbird image, values which are comparable to those generated strictly by human perceptions. As a point of note, when comparing results qualitative analysis values to their corresponding F-measure values, it was noticed that results which were classified as being of low quality, still yielded F-measure values which were still considered "good" or "acceptable" from the literature. Again, these results indicate that the proposed methodology is working as designed and is performing as well if not better than other methodologies.

One algorithmic consideration for the adjustment method regards the choice of buffer radius. For initial testing and evaluation the radius was chosen by considering the resolution of the image, the image size and trial and error. However, factors such as signal to noise ratio, homogeneity parameters, and an ultimate rationale behind choosing a buffer size were not used. In future work a rational method should be established which determines the buffer size by taking into consideration image size, image resolution, signal to noise ratio, and homogeneity parameters. In this vein another consideration was the choice of grid size. In this study, the grid size was chosen by considering the buffer size, and the size of the image. However, like buffer size a rational method, which takes into account those same factors, should be used in its determination. In line with that, it was acknowledged that if too large a grid size was selected, it would defeat the purpose of the grid. The same can be concluded about selecting a gird that was too small, the ranking scheme would then become irrelevant.

An additional algorithmic consideration concerns the adjustments of pixels which lay on the boundaries of the adjustment grid. Pixels which lay on the boarder of a grid square, could be adjusted several times when in principle it should be adjusted

only once. An acceptable solution to address this issue has not yet been presented and it is not known how this issue affects quality.

With regards to the incorporation of edge information, determining the weight of edge information, and noise considerations from the edge map requires investigation. For the purposes of this study, the weighting of the edge information was set to 1 in the energy function (equation 1), although a limited number of tests were also conducted in order to explore the effects of various edge weights. Tests where the weight was set to 0, illustrated the importance of incorporating edge information. Figure 6.2 shows the difference in adjustments when edge information was incorporated and when it was not. Using edge information was almost always beneficial to adjustments. Other tests showed that as the edge weight was increased to 2 it had a limited effect on adjustments until it reached a transition point around 3-4 where the edge information dominated the energy function and produced poorer results.

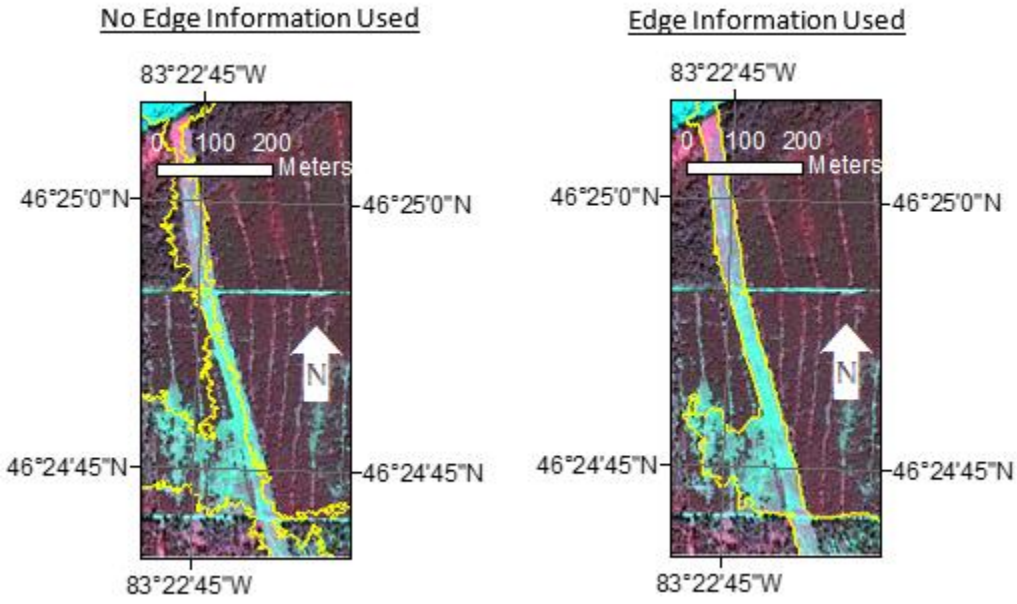

Figure 6.2. Adjustment results comparing the incorporation of edge information. No edge information used in the energy function (left) and edge information used in the energy function (right).

Regardless of the edge weight, when edge information was incorporated, it was observed that noisy edge maps could affect results by promoting noise driven adjustments as opposed to ones driven by actual edges. How the signal to noise ratio relates to the quality of results is not known and requires further investigation. More advanced, multi-scale or alternative approaches to producing edge maps should be investigated in further developments to address these concerns.

The elimination of the oscillating behaviour in pixel adjustments presents another algorithmic consideration. The point in which the algorithm determines when to be sensitive to the oscillating behaviour was determined through recording the number of adjustments per iteration and then checking if those adjustments were displaying asymptotic behaviour. If it was found that the adjustments have become asymptotic the program was allowed to become sensitive to recording and eliminating that oscillating behaviour. In future versions, a more advanced method to identify this behaviour should be explored, to allow the method to become more independent of user input, and more reliable.

With regards to segmentation results produced through the proposed adaptive segmentation technique, a number of considerations arise. The first was the selection of the segmentation parameters for the low resolution imagery. Choice of these parameters can impact greatly the final segmentation on the high resolution imagery. If segmentation of the low resolution imagery was too coarse training areas would encompass too many different land cover types and the segmentation of those areas, based on the parameters determined by the variogram analysis, would not be

suitable. Similarly, if the low resolution imagery was over segmented, the segmentation of the high resolution imagery would result in further over segmentation. At the time of this writing there are no automatic or more methodical ways of choosing the segmentation parameters of the low resolution imagery beyond user skill. For future work, a methodology should be developed which will allow for an acceptable segmentation of the low resolution imagery which will match results determined by user skill. This will not only decrease processing time but also create more consistency with testing.

Another consideration when operating the proposed segmentation technique was the determination of segmentation parameters with the variogram based method. It was found that a completely automatic selection of segmentation parameters can often lead to over and under segmentation of projected segmented areas, on the high resolution imagery. In order to combat this it was found that the best strategy involved an examination of both the segmentation parameters determined from the variograms, and the variograms themselves. Variograms were often examined to see if structures existed within them to imply multi-scale features, such as multiple sills, and the images themselves were often examined to see if areas exhibited over or under segmentation, based on the purely automatically determined segmentation

parameters. If over or under segmentation was seen the variogram determined segmentation parameters were manually adjusted based on the structures of the variogram. When these adjustments were done improvements to the segmentation of the high resolution imagery was seen. These tests show that implementing the variogram based method, for determining segmentation parameters, in a fully automatic fashion, was not as effective as when it was implemented with user input and oversight. This semi-automatic approach always out performs the automatic approach as presently implemented. In future work, alternative, fully automatic approaches to determining threshold parameters from the projected, adjusted, segments, should be investigated. Again, having a more automatic method to determining segmentation parameters will result in faster results, and also more consistency which will aid in analysis and further development.

In principle the proposed segmentation method can be applied to any two sets of images, one low resolution and one high resolution, as long as they are closely match with their co-registration. If co-registration is too coarse even with the boundary adjustment method, segmentation results from the low resolution image will begin to lose meaning. One aspect to the operation of the proposed method which requires consideration is the size of the image. The computation time is directly proportional

to the size of the area of the images to be segmented. For instance going from a 500 by 500 pixel image to a 1000 by 1000 pixel image results in at least a 4 time increase in computational time. As a final limitation and consideration with the developed image segmentation method regards the evaluation of the accuracy and quality of the segmentation results. At this time only user interpretation was used to evaluate the quality of the segments. Alternative approaches to evaluating the performance of this method should be investigated. Such as testing the method on imagery from segmentation test databases or user defined segment maps of preexisting test data. This would allow a more comprehensive evaluation of the method. Finally, tests should be done with other imagery sets, and also of different resolution levels, such as using very low resolution imager (250 m resolution) to aid in the segmentation of low resolution imagery (15-30m resolution) for comparison purposes.

6.2. CONCLUSIONS

In summary, a boundary adjustment method and an adaptive image segmentation method have been presented. The presented boundary adjustment method was successful in adjusting the boundaries of a segmentation map that was determined from a low resolution resampled Quickbird image or an ASTER image, projected

onto its corresponding Quickbird image. It was found that the resulting adjusted-segments had morphed into a configuration where the undesirable boundaries have been adjusted and the overall homogeneity of the segments in that image had been improved. The adjusted-segment map matched closely to the features from the Quickbird image. This method is innovative in two aspects. First, its utilization of a local buffer to determine single pixel adjustments based on minimizing an energy function, within a buffer. Second was the manner in which those adjustments were carried out, through local ranking, based on the greatest changes towards homogeneity, and the execution of those adjustments through the use of a grid which aided in grouping, ranking, and localizing those adjustments. The energy function was new as well; it integrated the energy functions used in the edge-based and region-based active contouring models. The presented multi-scale image segmentation method was also successfully implemented and tested on the same ASTER and Quickbird imagery. Segments determined from the ASTER imagery were successfully projected and adjusted onto the high resolution Quickbird imagery. Those projected and adjusted segments were successfully analyzed using a variogram based method to determine segmentation parameters, using both automatic and user driven techniques. Finally, the resulting segmentation maps of the high resolution imagery were deemed to be of suitable quality. The work

presented here can be used as a strong basis to develop/implement multi-scale and adaptive remote sensing segmentation techniques.

6.3. LOOKING FORWARD AND FUTURE WORK

The work presented in this thesis will act as the basis for several upcoming projects where effectively segmenting, and combining sets of images from different resolutions will be an essential step in their analysis. The objectives of these upcoming projects involve determining relationships between ground and arboreal lichen coverage and its corresponding spectral signature as measured from remotely sensed imagery, and innovative methodologies to combine radar and multispectral imagery for wetland identification. Effectively segmenting large images will be an essential step which this developed methodology will be an essential tool for.

From a development standpoint this work can be expanded upon in the following ways. The boundary adjustment methodology can be further developed by exploring a progressive approach to buffer size. Preliminary testing showed that during

adjustments, if the buffer was expanded in a progressive way, superior results would be produced. Formalizing this approach needs to be done and would be a natural extension to the work already completed. Another aspect to the boundary adjustment method which should be explored is utilizing more advanced edge detection and edge mapping methods. Testing has shown that results can vary depending on the level and style of edge maps which are used. It was suspected that the use of superior edge maps will result in superior adjusted results. As a final aspect to the adjustment method which should be further developed an alternative or more advance way of executing adjustments with regards to the grid system should be explored. A limitation to the grid system involves pixels which border several grids. These border pixels can be adjusted several times while in principle these pixels should be only adjusted once. An alternative approach should address this. With regards to the adaptive segmentation method, further testing and quantification of those tests would be a natural progression for its development. For instance, comparing segmentation results produced using the adaptive segmentation method to segmentation results produced by humans would be a good step to further evaluate methodology. In terms of development, exploring alternative methods to automatically determine segmentation parameters should be done. With the present version, using variogram analysis, segmentation parameters can be effectively

determined but on occasion requires adjustment which has made this iteration of the method only semi-automatic. Future work should be done with the objective to produce a fully automatic version of the method. Finally, further tests should be conducted using different sets of images to verify the operation of the method beyond forested scenes with medium and high resolution imagery.

Chapter 7

REFERENCES

1. Benz, U. C. P.; Hofmann, G.; Willhauck, I.; Lingenfelder, M.; Heynen, M. Multi-resolution, object-oriented fuzzy analysis of remote sensing data for GIS-ready information. *ISPRS Journal of Photogrammetry & Remote Sensing*, **2004,** 58, 239– 258.
2. Blaschke, T.; and J. Strobl, What's wrong with pixels? Some recent developments interfacing remote sensing and GIS. *GIS – Zeitschrift für Geoinformations systeme,* 2001, 6, 12-17.
3. Blaschke, T.; Burnett, C.; Pekkarinen, A. New contextual approaches using image segmentation for object-based classification. In: De Meer, F., de Jong, S. (Eds.), *Remote Sensing Image Analysis: Including the spatial domain*. Kluver Academic Publishers, Dordrecht, 2004, 211-236.
4. Yu, Q.; Gong, P.; Chinton, N.; Biging, G.; Kelly, M.; Schirokauer, D. Object based detailed vegetation classification with airborne high spatial resolution remote sensing imagery. *Photogrammetric Engineering & Remote Sensing*, **2006,** 72 (7), 799-811.

5. Burnett, C.; Blaschke, T. A multi-scale segmentation/object relationship modelling methodology for landscape analysis. *Ecological Modelling* **2003,** 168 (3), 233-249.
6. Chan,T.; Sandberg, B.; Vese, L. Active contours without edges for vector-valued images. *J. Vis. Commun. Image Represent.*, **2001,** 11 (2), 130–141.
7. DigitalGlobe, Inc., *Quickbird Imagery Products, Product Guide,* Longmont, Colorado, USA, 2006
8. Hu, B.; Judah, A., Multi-scale and adaptive segmentation of high-spatial resolution imagery, *Remote Sensing of Environment*, **2014** to be submitted.
9. Dey, V.; Zhang, Y.; Zhoug, M., A review on image segmentation techniques with remote sensing perspective, *Wagner W., Székely, B. (eds.): ISPRS TC VII Symposium – 100 Years ISPRS, Vienna, Austria, July 5–7, 2010, IAPRS,* Vol. XXXVIII, Part 7A
10. Thomas, N.; Hendrix, C.; Congalton, R. G. A comparison of urban mapping methods using high-resolution digital imagery. *Photogrammetric Engineering and Remote Sensing*, **2003,** 69(9), 963– 972.
11. Judah, A.; Hu, B.; Wang, J.; An Algorithm for Boundary Adjustment toward Multi-Scale Adaptive Segmentation of Remotely Sensed Imagery. *Remote Sensing*. **2014**, 6(5), 3583-3610.
12. Chan, T.; Vese, LA., Active contour and segmentation models using geometric PDE's for medical imaging. In: Geometric methods in bio-medical image processing. *Berlin: Springer*. **2002,** 63–75.
13. Cremers, D.; Rousson, M.; Deriche, R. A review of statistical approaches to level set segmentation: Integrating color, texture, motion and shape, *International Journal of Computer Vision*, **2007,** vol. 72, no. 2, pp. 195–215.
14. Gui, L.; Bresson, X.; Thiran, J. P.; 2005. Multiscale Image Segmentation Using Active Contours. *EPFL-REPORT*-87183
15. Kass, M.; Witkin, A.; Terzopoulos, D. Snakes: Active contour models. *Int. J. Comput. Vis.*, **1988,** 1, 321–331.
16. Wu, Q.; An, J.; Lin, B. A Texture Segmentation Algorithm Based on PCA and Global Minimization Active Contour Model for Aerial Insulator

Images, *IEEE Journal of Selected Topics in Applied Earth Observations and Remote Sensing*, **2012,** (5)5, October.

17. Zhang, K.H.; Song, H.H.; Zhang, L. *Active contours driven by local image fitting energy, Pattern Recognition*., **2010,** vol. 43, no. 4, 1199–1206.
18. Zhang, Y.; Matuszewski, B. J.; Shark, L.-K; Moore, C. J. Medical image segmentation using new hybrid level-set method, *BioMedical Visualisation, International Conference on Medical Information Visualisation*, **2008,** vol. 0, 71–76.
19. Tilton, J.; Lawrence, W. Interactive analysis of hierarchical image segmentation. *International Geoscience and Remote Sensing Symposium IGARSS-200*0, IEEE Press, New York, 733–73.
20. Chang, H-H.; Daniel, V.; Chu, W. Active Shape Modeling with Electric Flows, Visualization and Computer Graphics, *IEEE Transactions on* , **2010,** 16(5), 854,869.
21. Yuan, J.; Li, P.; Wen, Y.; Xu, Y. Level set segmentation of intensity inhomogeneous images based on local linear approximation of difference image, *Image Processing, IET* , **2012,** vol.6, no.5, 473,482.
22. Mishra, A. K.; Fieguth, P. W.; Clausi, D. A. Decoupled Active Contour (DAC) for Boundary Detection, *IEEE Transactions on Pattern Analysis and Machine Intelligence*., **2011,** vol. 33, no. 2, 310-324.
23. Nakhmani, A.; Tannenbaum, A. Self-crossing detection and location for parametric active contours, *IEEE Trans. Image Process.*, **2012,** vol. 21, no. 7, 3150–3156.
24. Campbell, J.; Wynne, R.; "Introduction to Remote Sensing", Guilford Publication; 2011
25. BlackBridge, *Satellite Imagery Product Specifications*, Version 6.0, November 2013
26. Lambert, J.; Sydney, P.; Africano, J.; SooHoo, V.; Hamada, K.; A Search For The Lost IDCSP Constellation, *19th Space Control Conference MIT Lincoln Laboratory*, April 2001

27. Baatz, M.; Schäp, M. Multiresolution segmentation An optimization approach for high quality multi-scale image segmentation. In: Strobl, J., Blaschke, T.; Griesebner, G.; *Angewandte Geographische Informations-Verarbeitung XII. Wichmann Verlag, Karlsruhe,* **2000,** 12-23.
28. Zhong, C.; Zhongmin, Z.; DongMei, Y.; Renxi, Ch. Multi-Scale Segmentation of The High Resolution Remotely Sensed Imagery, *Proc. IEEE Int. Geoscience Remote Sensing Symp.,*: **2005**, 3682-3684
29. Baatz, M.; Schape, A.; Nommemmacher, TF. Cognition network technology: Object orientation and fractal topology in biomedical image analysis – method and applications, *4th International Symposium on Fractals in Biology and Medicine Location: Ascona, Switzerland Date: MAR 10-13, **2004,*** 67-73
30. Happ, P.N.; Ferreira, R. S.; Bentes, C.; Costa, G. A; Feitosa, R. Q. Multiresolution segmentation: a parallel approach to high resolution image segmentation in multicore architectures, *The International Archives of the Photogrammetry, Remote Sensing and Spatial Information Sciences*, **2014,** Vol. XXXVIII-4/C7
31. Ward, J. H. Hierarchical grouping to optimize an objective function. *J. American Statistics Association*, **1963,** 58, 236-245
32. Hu, B.; Li, JL.; Jing, LH.; Judah, A. Improving the efficiency and accuracy of individual tree crown delineation from high-density LiDAR data, *International Journal of Applied Earth Observation and Geoinformation*, **2014,** 26, 145-155.
33. Garrigues, S.; Allard, D.; Baret, F.; Weiss,M. Quantifying spatial heterogeneity at the landscape scale using variogram models. *Remote Sensing of Environment*, **2006,** 103 (1): 81–96.
34. Li, PJ.; Cheng, T.; Guo, JC. Multivariate image texture by multivariate variogram for multispectral image segmentation. *Photogrammetric Engineering and Remote Sensing*, **2009,** 75 (2), 147-157

35. Woodcock, C.E.; Strahler, A.H.; Jupp, D.L.B. The use of variograms in remotesensing. 1. Scene models and simulated imaged, *Remote Sensing of Environment*, **1988,** 25 (3), 323-348.
36. Bruniquel-Pinel, V.; Gastellu-Etchegorry, J. -P. Sensitivity of texture of high resolution images of forest to biophysical and acquisition parameters. *Remote Sensing of Environment*, **1998,** 65, 61−85.
37. Curran, P. J., The semivariogram in remote sensing: An introduction. *Remote Sensing of Environment*, **1988,** 24, 493−507.
38. Lacaze, B.; Rambal, S.; Winkel, T. Identifying spatial patterns of Mediterranean landscapes from geostatistical analysis of remotely-sensed data. *International Journal of Remote Sensing*, **1994,** 15(12), 2437−2450.
39. Atkinson, P.M.; Lloyd, C.D. Non-stationary variogram models for geostatistical sampling optimisation: An empirical investigation using elevation data, *Computers and Geosciences*, **2007,** 33, 1285-1300
40. Karl, J.; Maurer, B. Spatial dependence of predictions from image segmentation: A variogram-based method to determine appropriate scales for producing land management information, *Ecological Informatics*, **2010,** 5, 194-202
41. Karl, J.; Maurer, B. Multivariate correlations between imagery and field measurements across scales: comparing pixel aggregation and image segmentation, *Landscape Ecology*, **2010,** 25: 591-605
42. Beauchemin M. Image thresholding based on semivariance, *Pattern Recognition Letters*, **2013**, 34, 456-462.
43. Estrada, F. J.; Jepson, A. D. Benchmarking Image Segmentation Algorithms, *International Journal of Computer Vision*, **2009,** 85, 167-181.
44. Chen, Y.; Jiao, X. Semivariogram fitting with linear programming. *Journal of Computer and Geosciences*, **1999,** 27, 71-76.
45. Abrams, M.; Hook, S.; Ramachandran, B.; (2004). ASTER User Handbook, Version 2. Jet Propulsion Laboratory, California Institute of Technology. Online:

http://asterweb.jpl.nasa.gov/content/03_data/04_Documents/aster_user_guide_v2.pdf

46. Canny, J. A computational approach to edge detection. *IEEE Trans. Pattern Analysis and Machine Intelligence*, **1986,** 8(6), 679–698.
47. Estrada, F. J.; Jepson, A. D. Benchmarking Image Segmentation Algorithms, *International Journal of Computer Vision*, **2009,** 85: 167-181.
48. Estrada, F. J.; Jepson, A. D. Spectral Embedding and Min-Cut for Image Segmentation, *British Machine Vision Conference*, London, U.K., 2005
49. Hu, B.; Li, J.; Jing, J.; Judah, A., Improving the efficiency and accuracy of individual tree crown delineation from high-density LiDAR data, *International Journal of Applied Earth Observation and Geoinformation*, **2014,** 26,145–155.
50. Arbelaez, P.; Maire, M.; Fowlkes, C., Malik, J., Contour detection and hierarchical image segmentation. *IEEE Trans. Pattern Anal. Mach. Intell.*, **2011,** *33*, 898–916.
51. Martin, D.R.; Fowlkes, C.C.; Malik, J. Learning to Detect Natural Image Boundaries Using Local Brightness, Color and Texture Cues, *IEEE Trans. Pattern Analysis and Machine Intelligence*, **2004,** 26(5), 530-549